Chemical Geology 284 (2011) 193–209

Contents lists available at ScienceDirect

Chemical Geology

journal homepage: www.elsevier.com/locate/chemgeo

Research papers

Influence of amorphous silica layer formation on the dissolution rate of olivine at 90 °C and elevated pCO_2

Damien Daval [a,b,c,*], Olivier Sissmann [a,b], Nicolas Menguy [d], Giuseppe D. Saldi [c], François Guyot [a,d], Isabelle Martinez [a], Jérôme Corvisier [b,1], Bruno Garcia [e], Imène Machouk [d], Kevin G. Knauss [c], Roland Hellmann [f]

[a] Institut de Physique du Globe de Paris, Centre de Recherches sur le Stockage Géologique du CO_2, 1 Rue Jussieu, 75238 Paris Cedex 05, France
[b] Laboratoire de Géologie, UMR 8538 du CNRS, École Normale Supérieure, 24 Rue Lhomond, 75005 Paris, France
[c] Earth Sciences Division, Lawrence Berkeley National Laboratory, MS 90R-1116, 1 Cyclotron Road, Berkeley, CA 94720, USA
[d] Institut de Minéralogie et de Physique des Milieux Condensés, CNRS, Universités Paris 6 et 7, 140 rue de Lourmel 75252, Paris, France
[e] IFP Energies Nouvelles, 1 et 4, avenue de Bois-Préau, 92852 Rueil-Malmaison Cedex, France
[f] Géochimie de l'Environnement, Laboratoire de Géophysique Interne et Tectonophysique, CNRS UMR C5559, OSUG, Université Joseph Fourier, 38041, Grenoble Cedex 9, France

ARTICLE INFO

Article history:
Received 29 November 2010
Received in revised form 20 February 2011
Accepted 21 February 2011
Available online 26 February 2011

Editor: J. Fein

Keywords:
Olivine
Carbonation
CO_2 sequestration
Passivation
Kinetic modeling

ABSTRACT

For mitigating against rising levels of atmospheric CO_2, carbonation of M^{2+}-bearing silicates has been proposed as a possible option for sequestering CO_2 over long time spans. Due to its rapid far-from-equilibrium dissolution rate and its widespread occurrence in mafic and ultramafic rocks, olivine has been suggested as a potentially good candidate for achieving this goal, although the efficacy of the carbonation reaction still needs to be assessed. With this as a goal, the present study aims at measuring the carbonation rate of San Carlos olivine in batch experiments at 90 °C and pCO_2 of 20 and 25 MPa.

When the reaction was initiated in pure water, the kinetics of olivine dissolution was controlled by the degree of saturation of the bulk solution with respect to amorphous silica. This yet unrecognized effect for olivine was responsible for a decrease of the dissolution rate by over two orders of magnitude. In long-term (45 days) carbonation experiments with a high surface area to solution volume ratio ($SA/V = 24{,}600\ m^{-1}$), the final composition of the solution was close to equilibrium with respect to SiO_2(am), independent of the initial concentration of dissolved salts (NaCl and $NaClO_4$, ranging between 0 and 1 *m*), and with an aqueous Mg/Si ratio close to that of olivine. No secondary phase other than a ubiquitous thin (≤40 nm), Si-rich amorphous layer was observed. These results are at odds with classic kinetic modeling of the process. Due to experimental uncertainties, it was not possible to determine precisely the dissolution rate of olivine after 45 days, but the long term alteration of olivine was indirectly estimated to be at least 4 orders of magnitude slower than predicted.

Taken together, these results suggest that the formation of amorphous silica layers plays an important role in controlling the rate of olivine dissolution by passivating the surface of olivine, an effect which has yet to be quantified and incorporated into standard reactive-transport codes.

Published by Elsevier B.V.

1. Introduction

Rising levels of atmospheric carbon dioxide (CO_2) have recently led the scientific community to devise potential strategies for carbon capture and storage (CCS) over long time spans. In that respect, one of the safest CCS options proposed is based on mineral trapping via the so-called carbonation process (Oelkers et al., 2008). The corresponding general reaction can be written as (M being a divalent metal):

$$M_xSi_yO_{x+2y-z}(OH)_{2z} + xCO_2 \rightarrow xMCO_3 + ySiO_2 + zH_2O \quad (1)$$

Such a reaction results in the chemical breakdown of a silicate mineral, release of silicon (at temperatures below 200 °C, essentially in the form of amorphous silica, see below), and consumption of CO_2, followed by its subsequent transformation to a solid carbonate precipitate (MCO_3). In aqueous media, the overall reaction above can be subdivided into two main steps: silicate dissolution and carbonate precipitation (e.g. Oelkers and Schott, 2005).

Various reasons potentially make olivine ($(Mg, Fe)_2SiO_4$) one of the best candidates for CO_2 sequestration purposes. First, olivine

* Corresponding author at: Present address: Earth Sciences Division, Lawrence Berkeley National Laboratory, MS 90R-1116, 1 Cyclotron Road, Berkeley, CA 94720, USA. Tel.: +1 510 486 7975; fax: +1 510 486 5686.
E-mail address: ddaval@lbl.gov (D. Daval).
[1] Present address: Mines Paris Tech, 35 Rue Saint-Honoré, 77305 Fontainebleau, France.

0009-2541/$ – see front matter. Published by Elsevier B.V.
doi:10.1016/j.chemgeo.2011.02.021

represents one of the most thermodynamically favorable minerals with respect to reaction (1) (e.g. Guyot et al., in press). Secondly, olivine is widespread in mafic and ultramafic environments: it is a common component of basalts, the main one of peridodites, and almost the only one of dunites. Moreover, natural evidence for carbonate formation associated with (and/or resulting from) the weathering of olivine has been previously reported (e.g. Kelemen and Matter, 2008; Andreani et al., 2009; Beinlich et al., 2010). Finally, olivine is presumably one of the fastest dissolving Mg-bearing minerals (Guyot et al., in press), which represents the initial step of the overall carbonation process.

Owing to its rapid dissolution kinetics (Luce et al., 1972; Blum and Lasaga, 1988; Wogelius and Walther, 1991, 1992; Jonckbloedt, 1998; Awad et al., 2000; Chen and Brantley, 2000; Pokrovsky and Schott, 2000a,b; Rosso and Rimstidt, 2000; Oelkers, 2001; Liu et al., 2006; Davis et al., 2009; Daval et al., 2010b), its geological relevance, and its simple chemical composition and structure, a growing number of studies have been dedicated to better constraining the rate and mechanism of olivine carbonation. While a few studies focused exclusively on either of the two main steps of the carbonation process at conditions relevant for CO_2 sequestration (see Hänchen et al., 2006; Prigiobbe et al., 2009 for olivine dissolution at high pCO_2; Hänchen et al., 2008; Saldi et al., 2009; Ballirano et al., 2010 for carbonate formation and stability), the vast majority of them addressed the overall process by running batch experiments using Mg-rich olivine close to forsterite (Mg_2SiO_4) composition as starting materials (e.g. O'Connor et al., 2002; Giammar et al., 2005; Bearat et al., 2006; Chen et al., 2006; Gerdemann et al., 2007; Dufaud et al., 2009; Jarvis et al., 2009; Garcia et al., 2010; King et al., 2010). Such investigations yielded interesting first-order results, with some of the main important findings being summarized as follows:

(i) The optimal carbonation conditions were determined to be around 185 °C and $pCO_2 = 15$ MPa (e.g. Gerdemann et al., 2007), the extent of carbonation, defined as the degree of stoichiometric conversion of the silicate to the carbonate, leveling to a maximum value slightly above 80%. The reasons for a decrease of the carbonation efficiency at higher temperatures is not straightforward, but may be due to competition between carbonation and serpentinization reactions, as suggested by the results reported in Dufaud et al. (2009) or King et al. (2010).

(ii) For a given temperature, an optimum extent of carbonation is obtained by increasing both the alkalinity and the salinity of the aqueous solution (0.64 M $NaHCO_3$ + 1 M NaCl) (O'Connor et al., 2002). Conversely, it has been clearly shown that in the acidic pH range, the dissolution rate of olivine decreases as pH increases (see Table 1). As a consequence, the results from O'Connor et al. (2002) suggest that the optimal pH and alkalinity conditions represent a compromise between promoting the magnesite precipitation step, without lowering too much the dissolution rate of olivine. This finding may indicate that the rate-limiting step of olivine carbonation is not 'simply' the dissolution step. Recent data on magnesite precipitation rates seem to support this idea. For instance, Giammar et al. (2005) found that magnesite nucleation was not observed for saturation indices as high as 1.14 at 95 °C. Moreover, Saldi et al. (2009) reported that the rate constant of magnesite growth at 100 °C is 6 orders of magnitude lower than that of calcite at conditions where precipitation rates are controlled by the same mechanism (spiral growth). Furthermore, although possibly faster than magnesite precipitation, the formation of hydrated Mg-carbonates from supersaturated solutions remains a process much slower than that of Ca-carbonates under similar conditions (Hänchen et al., 2008), emphasizing that determining *a priori* the rate-limiting step of the carbonation of Mg-silicates is challenging.

(iii) In addition to the very slow precipitation rate of Mg-carbonates, several studies reported that blocking of the carbonation reaction could indeed take place upstream, during the dissolution step. Based on the results from Bearat et al. (2006) and Jarvis et al. (2009), the formation of a passivating silica layer could prevent fluid from reaching the pristine olivine reaction front, thereby inhibiting the continued dissolution of olivine. Interestingly, this result is at odds with the observations of Daval et al. (2009b), who showed that the occurrence of amorphous silica layers formed on the surface of wollastonite did not significantly affect its dissolution rate. This emphasizes the idea that the properties of silica coatings are not universal, but rather may depend on the structure and composition of the parent mineral and/or on the experimental conditions (i.e. $T = 185$ °C, $pCO_2 = 13.5$ MPa, starting solution = 0.64 M $NaHCO_3$ + 1 M NaCl for Bearat et al. (2006) vs. $T = 90$ °C, $pCO_2 = 25$ MPa, starting solution = ultrapure water for Daval et al. (2009b)).

The present study aims at bringing new constraints on the rate-limiting step of the carbonation of forsterite olivine. The originality of the present study is based on the following points:

(i) With the exception of the study by Giammar et al. (2005), all the abovementioned studies dealing with forsterite carbonation were run at temperatures significantly above the usual upper bound for in situ geological storage of CO_2 (~100 °C, e.g. Bachu, 2000), and are rather representative of ex situ CO_2 sequestration methods. In addition, most of these studies were run in alkalinized solutions, which could be used for ex situ CO_2 sequestration purposes, but which are less relevant for in situ CO_2 sequestration. As a consequence, our experiments were run at 90 °C and pCO_2 ranging from 20 to 25 MPa, corresponding to more realistic P–T conditions of CO_2 storage. Moreover, because some sequestration projects using basalts foresee the co-injection of seawater with CO_2 (Gislason et al., 2010), some

Table 1
Compilation of dissolution kinetic parameters for forsteritic olivine determined at far-from-equilibrium conditions.

Source	T range	pH range	n	E_a	k_0	k_{90}	Runs
Blum and Lasaga (1988)	25	2.0–5.0	0.56	n.d.**	4.17E+03	1.08E−05	8
Wogelius and Walther (1992)	25–65	2.0–6.0	0.54	79.5	7.74E+06	2.84E−05	7
Chen and Brantley (2000)	65	2.0–5.0	0.71	n.d.**	2.63E+04	6.80E−05	8
Pokrovsky and Schott (2000b)	25	1.0–6.0	0.50	n.d.**	6.62E+03	1.71E−05	34
Rosso and Rimstidt (2000)	25–45	1.8–3.8	0.50	42.6	3.47E+00	2.59E−06	28
Oelkers (2001)	25–65	2.0	n.d.*	63.8	2.39E+04	1.59E−05	26
Hänchen et al. (2006)	90–150	2.0–8.5	0.45	52.9	8.54E+02	2.10E−05	24

The parameters were reported from studies performed at acidic conditions, in organic ligand-free solutions, for the T and pH ranges listed in the 2nd and 3rd columns. The far-from-equilibrium dissolution rate law is written according to the expression: $r = k_0 \times \exp(-E_a / RT) \times a_{H^+}^n$ with $k_{90} = k_0.\exp(-E_a/(363R))$. The activation energy (E_a) is indicated in kJ.mol^{-1}, and the rate constants are expressed in mol.m^{-2}.s^{-1}. The last column indicates the number of individual experiments run to establish the rate law. *pH-dependence not determined in this study (study run at a unique pH condition only). ** Activation energy not determined from these studies (study run at one temperature only). Consequently, the k_{90} values reported in this table were calculated by merging the activation energies determined in the other studies (average value: 59.7 kJ/mol).

of the experiments in our study were run with various NaCl concentrations in order to determine whether salinity has an impact on the carbonation process.

(ii) Although it has been qualitatively suggested in previous higher temperature studies that the formation of silica coatings may slow down the transport of dissolved species to/from the reactive surface of olivine (Bearat et al., 2006; Jarvis et al., 2009), this effect has neither been quantified so far, nor compared with simple models using geochemical codes. As a consequence, this question is addressed in the present study, and the consequences for long-term olivine alteration in confined environments are assessed, by preliminary nm-scale analyses of the interfacial region of the weathered olivine mineral.

(iii) Finally, the non-universal behavior of silica coatings that form on various minerals and at different physicochemical conditions are evoked, and the mechanistic origin for the observed discrepancies are discussed.

2. Materials and methods

2.1. Starting materials

The present study involved two independent types of experiments which were run in two different locations (Laboratoire de Géologie, ENS, Paris, France and Earth Sciences Division, LBNL, Berkeley, CA, USA). Hence, there were slight differences in the protocols for preparing the starting materials, and two batches of olivine were purchased from different sources (Mineral K and Wards Natural Science). Both batches originated from San Carlos (Arizona, USA) and consisted of cm-sized translucent, bottle-green crystals of gem quality. With the exception of minor quantities of iron oxides resulting from superficial weathering (that were easily removed manually), no other minor phases were evidenced with the analytical techniques we used (i.e., Raman spectroscopy, X-ray diffraction, scanning electron microscopy). The chemical compositions of the two batches were determined by electron microprobe and are listed in Table 2. These measurements indicate that the average compositions were $(Mg_{0.88}Fe_{0.12})_2SiO_4$ and $(Mg_{0.91}Fe_{0.09})_2SiO_4$ respectively, when normalized to four oxygens. Such results are consistent with the range of compositions determined in previous studies (Fo_{88-92}). Samples were initially crushed and sieved to recover the 100–300 (ENS experiments) and 149–295 (LBNL experiments) μm-sized fractions. The powders were then ultrasonically cleaned in ethanol for 10 min in order to remove fine particles, with the cloudy supernatant being removed and replaced with fresh ethanol. This process was repeated up to 10 times until the supernatant became clear. The olivine was then rinsed with ultrapure deionized water (18.2 $M\Omega.cm^{-1}$) for 5 min and dried overnight in air at 60 °C. The efficacy of this procedure was monitored by scanning electron microscopy (SEM), which revealed only a few fine particles still adhering to the surface. The specific surface area (SSA) of the powders was determined to be 0.041 $m^2.g^{-1}$ for the 100–300 μm-sized fraction and 0.015 $m^2.g^{-1}$ for the 149–295 μm-sized fraction using a three-point BET method with Kr as the absorbent gas.

2.2. Experimental equipment and protocols

2.2.1. High SA/V experiments

The experiments performed with high olivine surface area (SA) to solution volume (V) ratios involved the batch of Fo_{88} forsterite (grain size: 100–300 μm), and were carried out at the ENS. Because the set-up we used was thoroughly described previously in Daval et al. (2009a), only the most important features are detailed here. The investigations were conducted at $T = 90$ °C and $pCO_2 = 25$ MPa in small Teflon capsules (volume ~3 ml) capped with porous alumina plugs, and stacked in a Ti-autoclave. At these conditions, CO_2 is supercritical, and was free to diffuse across the alumina plugs covering the capsules. Although the use of batch reactors considerably complicates the quantification of the feedback between the evolution of the solution chemistry and reaction rates, they arguably better simulate natural in situ carbonation conditions, and are especially useful for examining the coupled effect of silicate weathering and secondary coating formation.

Each capsule was filled with a small amount of olivine powder (~300 mg) and ultrapure deionized water (~0.5 ml), corresponding to $SA/V = 24{,}600\ m^{-1}$. Runs were terminated after different time durations (ranging from 24 h to 45 days) to follow the extent of reaction as a function of time (based on both solid and solution analyses, see section 2.3). From 2 to 11 capsules per run were dedicated to the investigations gathered in the present study, each one being physically and chemically isolated from its closest neighbors (Daval et al., 2009a). For long-term experiments (45 days), some of the capsules were filled with NaCl or $NaClO_4$ solutions with different concentrations (0.01; 0.1; 1 m). The use of these two solutes enabled us to evaluate whether the catalytic effect of NaCl reported in some previous carbonation studies (e.g. O'Connor et al., 2002) involved an ion-specific mechanism (Cl^-) or the ionic strength itself (see a similar protocol in, e.g. Sidhu et al., 1981).

2.2.2. Low SA/V experiment

The high SA/V experiments were useful for better understanding the long-term behavior of olivine carbonation. Conversely, the initial dissolution rate of olivine at such conditions is extremely rapid, such that it was not possible to measure the rates before the attainment of saturation with respect to amorphous silica. Moreover, as described by Daval et al. (2009a), the sampling of the experimental fluids was not possible without first stopping, and thus quenching these experiments, a process which took up to 1.5 h. This protocol has two major weak points: first, it is not suitable for studying reactions with time durations of less than a few hours; secondly, because the quench is not instantaneous, the recovered fluid at ambient conditions may not have exactly the same composition as at in situ conditions (see section 3.1.2 and an in-depth discussion of this effect in Daval et al., 2009a). To compensate for these disadvantages, we ran a complementary experiment in an apparatus suitable for determining accurately the dissolution rate of olivine during the early stage of the carbonation process, i.e. under conditions undersaturated with respect to amorphous silica.

The corresponding experiment, conducted at LBNL, was run at a low SA/V ratio using a batch of Fo_{91} forsterite (grain size: 149–295 μm) described above. We used a Dickson-type autoclave, whose extensive description can be found elsewhere (e.g. Seyfried et al., 1979; Knauss and Copenhaver, 1995). Briefly, the reaction took place in a flexible Au bag (220 ml) fitted with a removable Ti closure. A Ti sampling tube attached to the closure, which incorporates a standard high pressure tube fitting, exits through the head of the apparatus. A leak-tight seal was achieved by compressing the top of the gold bag against a flared portion of the Ti head. At the start of the run, the Au bag was filled with 185 ml of ultrapure deionized water and 3.0629 g of olivine, corresponding to $SA/V = 248\ m^{-1}$ (2 orders of magnitude smaller than for the previous experiments). The Au bag/Ti closure seal was then tested by pressurizing the assembly and immersing it in water. The assembly was subsequently introduced into a large stainless steel high pressure vessel (845 ml) filled with deionized water beforehand. The pressure outside the bag was brought to 20 MPa at ambient temperature by pumping deionized water with a syringe pump. Finally, 17 ml of liquid CO_2 was injected inside the Au

Table 2
Chemical composition of the two different olivine batches determined from electron microprobe analysis (in wt.%).

	SiO_2	CaO	MnO	FeO	NiO	MgO	total
ENS	40.89	0.09	0.09	9.18	0.4	49.32	99.97
LBNL	40.77	0.12	0.15	11.19	0.37	47.81	100.41

bag at ambient temperature and 20 MPa with a second pump; the corresponding excess of water outside the bag being withdrawn using the first syringe pump in 'constant pressure' mode. The amount of CO_2 injected was chosen such that the water phase would remain equilibrated with a headspace of CO_2 under the run conditions, regardless of the amount of CO_2 consumed during carbonation.

The stainless steel vessel was then loaded into one of the two furnaces of a dual-furnace rocking autoclave system (CoreTest Systems, Inc.). The temperature was increased to 90 °C, and the pressure was held constant by the use of a syringe pump operating in 'constant pressure' mode at 20 MPa, close to the maximum working pressure of this pump. The autoclaves were rocked daily to avoid potential chemical gradients in the liquid phase. This set-up enabled continuous sampling of the aqueous phase with time without having to interrupt the experiment. A typical sampling procedure took about 10 min and consisted of collecting 3 aliquots (1–1.5 ml each) per sampling day. The first one was systematically discarded, the second was dedicated to qualitative pH measurement at ambient conditions, and the last one was used for analyzing the solution chemistry.

Despite slight differences between the two types of experiments, namely the very small difference in chemical composition of the olivine and the pCO_2 (note that the 5 MPa difference does not significantly affect the chemistry of the starting solutions, see section 2.4), it is reasonable to assume that when taken together, all of the experiments in the present study (inclusive of variable *SA/V* ratios) have been used to address, quantify, and characterize a single process, namely, the carbonation rate of San Carlos olivine at 90 °C and elevated pCO_2, and the corresponding links to the solution chemistry and the formation of secondary phases.

2.3. Characterization and analytical procedures

2.3.1. Fluid analyses

For each type of experiment, either after quenching (ENS) or in situ sampling (LBNL), the aqueous samples were filtered through a PTFE filter with a pore size of 0.22 μm, diluted at least 10 fold in ultrapure water and acidified with HNO_3 2%. The samples were then analyzed either by ICP-AES (ENS) or ICP-MS (LBNL) for Mg, Fe, and Si. The analytical uncertainties in the measurements were better than 5%, based on repeated analyses of standard solutions and blanks.

2.3.2. Bulk solid analyses (ENS experiments)

X-ray diffraction (XRD) data were collected with a Rigaku ultraX18HFCE Bragg–Brentano diffractometer equipped with a rotating copper anode (Cu Kα radiation). The conditions for generating the X-ray beam were 300 mA and 50 kV. Scans were taken for 2θ ranges from 10 to 70° with 0.01°/s steps, with total accumulation times of 100 min. The detection limit of XRD is close to ~1%. However, because only limited carbonate formation is expected at such temperatures (e.g. Giammar et al., 2005), complementary analyses were performed using a Rock-Eval 6 apparatus. The operation and performance characteristics of the Rock Eval technique can be found in Lafargue et al. (1998) and Behar et al. (2001). Basically, 200 mg aliquots of reacted powders were heated in air to 850 °C at a heating rate of 20 °C/min. This leads to the thermal decomposition of carbonate minerals contained in the samples according to the reaction:

$$MCO_3 \xrightarrow{\Delta} MO + CO_2 \quad (2)$$

The CO_2 produced is then quantified using an infra-red analyzer in a continuous on-line mode. The temperature for maximum CO_2 production depends on the carbonate, specifically the chemical composition and the nature of chemical bonds between the cations and the CO_3^{2-} groups (Lafargue et al., 1998). Thus, the thermal decomposition maximum can be used to determine the chemical composition of the carbonates present in the samples (~650 °C for magnesite, e.g. Garcia et al., 2010). The quantification limit of the Rock Eval technique is ~0.02 wt.% C, corresponding to ~0.15 wt.% $MgCO_3$ (i.e. this technique is one order of magnitude more sensitive than XRD).

2.3.3. Microscopic observations

The powders were recovered at the end of each experiment, fixed on an adhesive carbon support, gold-coated, and then studied by SEM (Hitachi S-2500) operating at 15 kV and a working distance of 25 mm. Qualitative chemical analyses were acquired by energy dispersive X-ray analysis (EDS, Thermo Noran Si/Li detector).

To obtain preliminary insights into the structure and chemistry of the olivine/water interface, two ultrathin electron transparent cross sections were prepared by focused ion beam (FIB) milling on an olivine grain (batch 45-04, see Table 3) that was reacted for 45 days. The sample surface was re-metalized beforehand with a carbon coat to minimize potential artifacts due to Pt and Ga ion beam interactions during the milling process (see, e.g., Lee et al., 2007). The FIB milling was performed either with a FEI Model 200 SEM FIB or a Zeiss Neon EsB40 FIB/FEG-SEM system; details of the procedure can be found in Daval et al. (2009b). The FIB thin sections were then observed by transmission electron microscopy (TEM) using high-resolution transmission electron microscopy (HRTEM) and scanning transmission electron microscopy (STEM) observations with a JEOL 2100F (FEG) operated at 200 kV. STEM observations were performed both in brightfield (BF) and darkfield (DF) modes. EDXS maps were acquired in STEM DF mode, with a focused electron beam (1 nm).

2.4. Thermodynamic calculations and kinetic modeling

The fugacity of CO_2 was estimated to equal ~13.5 and ~11.5 MPa for the experiments run at 25 and 20 MPa, respectively. This calculation was based on fugacity coefficients (Γ_{CO_2}) given by Spycher et al. (2003) that correspond to our in situ *P–T* conditions. The starting pH and dissolved CO_2 concentrations were calculated with the geochemical code CHESS (van der Lee and De Windt, 2002) using the LLNL EQ3/6 database. The logarithms of the formation constants are listed in the CHESS database, and are used to compute by interpolation the formation constant for any temperature between the minimum and maximum temperature provided by the polynomial expression. Activity coefficients for aqueous species were calculated using the Davies equation. The electrical balance was ensured using pH as an adjustable parameter. For the ENS experiments, the starting pH was 3.07 and $[CO_2(aq)] = 1.56\ m$, whereas for the LBNL experiment, the starting pH was 3.11 and $[CO_2(aq)] = 1.35\ m$. These values show that the initial solution chemistries were almost equivalent in all experiments. The aqueous magnesium and silica concentrations served as input to the geochemical code CHESS for computing the in situ pH and saturation indices of the solid phases. The CHESS code was also used to independently model the release rates of magnesium in the ENS experiments using dissolution data from the literature. A commonly used general kinetic expression that links the kinetics of reaction to the major rate-controlling parameters (e.g. Lasaga, 1995):

$$r = k_0 \exp(-E_a / RT) A_{min}\, g(I)\, \Pi a_i^{ni} f(\Delta G_r) \quad (3a)$$

is implemented in the kinetic module of the code as follows (adapted from van der Lee and De Windt, 2002):

$$r = \pm k_0 \exp(-E_a / RT)\, A_{min}\, \Pi a_i^{ni} \left(1 - \left(Q / K_{eq}\right)^{\mu}\right)^{\lambda} \quad (3b)$$

In these equations, r is the overall dissolution/precipitation rate ($mol.s^{-1}$), negative values indicating dissolution, and positive values precipitation, k_0 ($mol.m^{-2}.s^{-1}$) is the rate constant that incorporates

Table 3
Summary of the results obtained for high *SA/V* experiments.

Sample	Solution	m_0	m_f	V	[Si]	[Mg]	ΔG_r(sil)[1]	ΔG_r(mag)[1]	ΔG_r(for)[1]	ΔG_r(sil)[2]	ΔG_r(mag)[2]	%C
1 day												
01-02	Ultrapure water	0.2902	0.2898	0.498	5.4	8.8	−0.2	−4.0	−73.2	2.0	13.9	0.00
01-15	Ultrapure water	0.2948	0.2893	0.498	4.6	9.3	−0.7	−3.9	−74.2	1.4	13.9	0.00
5 days												
05-04	Ultrapure water	0.3011	0.2953	0.508	4.7	9.3	−0.6	−3.9	−76.2	1.6	13.9	0.00
05-10	Ultrapure water	0.2872	0.2846	0.486	5.5	8.3	−0.1	−5.4	−77.4	2.2	13.3	0.00
15 days												
15-08	Ultrapure water	0.2882	0.2861	0.491	4.8	8.3	−0.6	−5.4	−77.8	1.8	13.3	n.d.
15-16	Ultrapure water	0.2916	0.2865	0.493	4.2	5.9	−0.9	−7.9	−83.3	1.6	11.6	0.00
15-18	Ultrapure water	0.2904	0.2859	0.510	4.7	7.8	−0.6	−5.8	−78.8	1.6	13.1	0.00
20 days												
20-00	Ultrapure water	0.2999	0.2991	0.500	5.7	10.3	−0.1	−3.7	−74.5	2.1	14.4	n.d.
20-10	Ultrapure water	0.2902	0.2898	0.498	4.0	22.6	−1.1	1.4	−65.5	1.0	17.5	0.00
45 days												
45-00	Ultrapure water	0.2665	0.2602	0.497	4.8	9.9	−0.5	−4.0	−75.3	1.8	14.1	0.00
45-11	Ultrapure water	0.2921	0.2914	0.493	4.4	13.8	−0.8	−1.7	−70.7	1.5	15.5	0.00
45-18	NaCl 0.01 *m*	0.2921	0.2908	0.515	5.5	8.7	−0.1	−6.1	−82.3	1.8	13.7	0.00
45-13	NaCl 0.10 *m*	0.2943	0.2939	0.499	5.3	9.4	−0.2	−7.5	−85.1	1.0	12.8	0.00
45-04	NaCl 1.00 *m*	0.2801	0.2894	0.500	4.8	9.0	−0.5	−10.2	−90.8	−1.5	9.9	0.00
45-10	NaCl 1.00 *m*	0.3311	0.3391	0.513	4.9	13.9	−0.5	−5.2	−77.6	−1.7	12.1	0.00
45-18b	$NaClO_4$ 0.01 *m*	0.2987	0.2958	0.503	5.4	13.2	−0.1	−2.2	−71.6	1.8	13.4	0.00
45-04b	$NaClO_4$ 1.0 *m*	0.2563	0.2719	0.471	4.2	7.0	−0.9	−10.5	−88.6	−1.0	7.9	0.00
45-16	$NaClO_4$ 1.0 *m*	0.3104	0.3077	0.508	4.2	7.7	−0.9	−9.7	−86.9	−1.1	8.6	n.d.

The first two columns indicate the name of the sample and the chemical composition of the starting solution. The three following columns contain, respectively, the masses of the powders before (m_0) and after (m_f) experiment (in g) and the volume (ml) of the aqueous solution. The columns labeled [Si] and [Mg] indicate the aqueous concentrations of SiO_2 (aq) and Mg^{2+} measured by ICP-AES (mmol.L^{-1}). The five following columns give the values of Gibbs free energy of dissolution (kJ.mol^{-1}) of SiO_2(am) (sil), magnesite (mag), and forsterite (for) either (1) at T = 90 °C, pCO_2 = 25 MPa, or (2) at ambient conditions (T = 25 °C, pCO_2 = 3.8E−05 MPa). The last column reports the measured amounts of mineral carbon (in wt.% C).

pre-exponential factors in the Arrhenius relation, E_a is the activation energy (J.mol^{-1}), R and T are the gas constant (J.mol^{-1}.K^{-1}) and temperature (K), respectively, A_{min} is the reactive surface area (m^2). The $g(I)$ term in Eq. (3a) conveys a possible dependence of the rate on the ionic strength (I) of the solution, but is not taken into account by the CHESS code. The Πa_i^{ni} term expresses the rate effect of aqueous species that catalyze or inhibit the overall reaction (including H^+). Note that values of k_0, E_a, n_i were taken from the literature for olivine dissolution and are listed in Table 1. The $f(\Delta G_r)$ term in Eq. (3a) is a function that describes the dependence of the rate on the Gibbs free energy of the reaction (ΔG_r). In the CHESS code, this function is implemented as $f(\Delta G_r) = (1-(Q/K_{eq})^{\mu})^{\lambda}$, where Q is the activity product of the reaction and K_{eq} is the corresponding equilibrium constant. The exponents n_i, μ and λ are parameters generally determined experimentally. For olivine dissolution, as for many minerals, μ and λ are unknown, and are thus assigned values of unity, as in most modeling studies (e.g., Xu et al., 2004; Knauss et al., 2005; Daval et al., 2009a, 2010b). In this case the term $f(\Delta G_r) = (1-Q/K_{eq})$ describes the free energy-dependence of the reaction within the framework of transition state theory (TST) (e.g. Lasaga, 1981). Even though the relevance of such a formalism has been recently criticized (e.g. Hellmann and Tisserand, 2006; Daval et al., 2010a; Hellmann et al., 2010), it is worth noting that to the best of our knowledge, no alternative formulation is available for olivine.

3. Results

3.1. High SA/V experiments

3.1.1. Estimation of magnesite content and microscopic observations

No crystalline secondary phases were detected by XRD for any of the reacted olivine powders recovered between the 1st and the 45th day of reaction. Because the quantification limit of XRD is limited to ~1% wt., additional measurements were realized using the Rock-Eval technique. As reported in Table 3, if present, the amount of Mg-carbonate formed during the experiment is below the quantification limit of this technique (~0.15 wt.% $MgCO_3$). The SEM observations confirmed the absence of Mg-carbonates. However, they occasionally revealed the occurrence of sparse, nm-sized phases relatively richer in Fe than olivine (appearing as a lighter color when imaged in backscattered electron mode). These sparsely occurring precipitates may be Fe(III) (hydr)oxides, rather than Fe-carbonates, which would be consistent with results shown in previous studies (e.g. Chen and Brantley, 2000; Giammar et al., 2005; Andreani et al., 2009), where no attempt was made to remove O_2(aq) from the initial solution, as well.

The SEM images revealed that the surfaces of olivine grains are non-homogeneously covered by small, shallow irregular etch pits (Fig. 1). When the reaction was initiated in NaCl rich solutions, some μm-sized crystals were identified, whose chemical composition is consistent with that of halite (inset in Fig. 1). Because the solution was not saturated with respect to halite under both run and ambient conditions, it is very likely that these crystals resulted from the evaporation of small amount of residual solution remaining on the olivine grains upon recovery.

To minimize sampling bias effects with respect to the TEM observations of the reacted grains, two separate thin sections from one reacted grain (sample 45-04) were prepared by FIB and observed by TEM. Observations based on each separate TEM foil are described next.

With respect to the first thin-section, no secondary phase other than a ubiquitous, thin amorphous layer was observed (Fig. 2a). The thickness of this layer varies along the interface, ranging from 15 to 40 nm. The olivine lattice fringes terminate abruptly at the interface with the amorphous layer. The crystalline-amorphous interface often displays a 'scalloped' nature (Fig. 2a and b). Based on Fig. 2b, there is no obvious evidence for porosity within amorphous silica layer, as opposed to what was stated in Cailleteau et al. (2008) or Daval et al. (2009b), who used similar methods to probe surface layers on

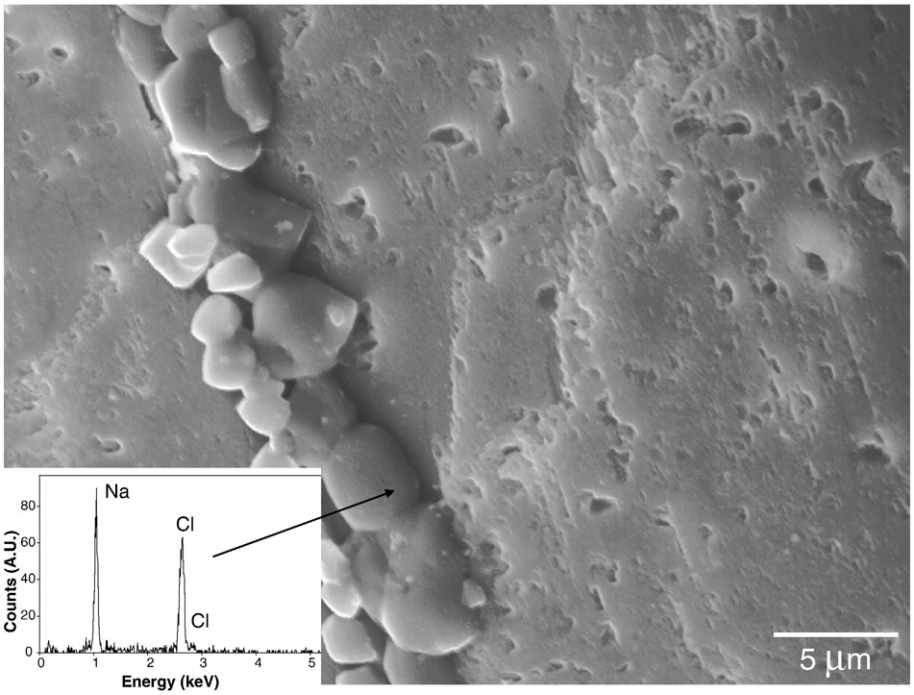

Fig. 1. Surface of a selected grain of olivine from experiment 45-04, revealing etch pits and other surface corrosion features. The crystals precipitated on the surface have a NaCl composition (see corresponding EDX analysis in inset) and were presumably formed at the end of the experiment after evaporation of the reactant solution (see text for details).

weathered glass and wollastonite, respectively. The bulk chemical composition of the amorphous phase revealed by EDXS analyses is consistent with a silica-rich phase containing minor amounts of Mg (Fig. 2c). To better probe the chemistry of the interfacial region, STEM-EDX profiles were measured perpendicular to the interface. The particular profile shown in Fig. 2d reveals a 50 nm-wide sigmoidal decrease in the Mg concentration from the olivine interface to the top of the silica layer. All other profiles (not shown) in the same general region did not produce sharper gradients. Moreover, it is also worth noting that despite many attempts, it was not possible to measure a sharp gradient for Pt, which in theory, should be sharp, since it was a deposited overlayer. A typical measured Pt gradient is 25–30 nm wide; this provides information on the nature of the Mg gradient, which is subject to further discussion (see section 4.3 and Appendix). The possibility that some of the sigmoidal nature of the profile is an artifact cannot be fully discounted.

With respect to the second thin section, the amorphous silica coating was also very thin, with thicknesses up to 20 nm. As with the first thin section, there was no apparent nm to µm-sized porosity. In contrast to the first thin section, the amorphous layer was less continuous, but could still be clearly seen (Fig. 3a, and the corresponding fast Fourier transform (FFT) shown in Fig. 3d). Due to the irregular nature of the termination of the lattice fringes of the olivine along the crystalline-amorphous interface, we did not attempt to measure the chemistry along a STEM-EDX line scan. In some localized interfacial areas, the olivine crystal was progressively disordered (see FFT of selected areas in Fig. 3b–d). This is reflected in the broader nature of the diffraction spots shown in Fig. 3c, as compared to Fig. 3b (bulk crystal).

3.1.2. Solution chemistry at the end of each run

The chemical compositions of the solutions at the end of each experiment are listed in Table 3. The average Mg concentrations were: 9.1 ± 0.4, 8.8 ± 0.7, 7.4 ± 1.3, 16.2 ± 6.4, and 10.3 ± 2.7 mmolal after 1, 5, 15, 20, and 45 days, respectively. The confidence intervals indicated here represent the standard deviation to the mean value of the concentrations measured in the different aliquots. A regression of the abovementioned average concentration values against time reveals that there is no statistically relevant linear evolution of the Mg concentration with time ($r^2 = 0.02$). Moreover, the final Mg concentrations of the solutions initially enriched in either NaCl or $NaClO_4$ are indistinguishable from those experiments starting with pure water.

The average Si concentrations were: 5.0 ± 0.6, 5.1 ± 0.6, 4.6 ± 0.3, 4.9 ± 0.9, and 4.8 ± 0.5 mmolal after 1, 5, 15, 20, and 45 days, respectively. As for the Mg concentrations, the concentrations of Si were constant with respect to time and independent of the initial solution composition.

To further understand these apparent steady-state Mg and Si concentrations, the Gibbs free energies with respect to the dissolution of key solid phases were calculated both for experimental in situ and ambient conditions, and are reported in Table 3. The first observation is that the calculated ΔG_r values with respect to forsterite dissolution are representative of what has always been classically considered as 'far-from-equilibrium' conditions, ranging from -90.8 to -65.5 kJ.mol^{-1}. These values indicate that thermodynamic equilibrium with olivine was never reached in any of the capsules, such that the continuation of olivine dissolution is thermodynamically feasible. Moreover, these calculations showed that, with the exception of sample 20–10, the extent of olivine dissolution was never large enough to reach saturation with respect to magnesite under run conditions. This observation is thus consistent with the abovementioned absence of Mg-carbonates in the reacted powders. Finally, the Si concentrations at in situ experimental conditions are very close to, but systematically below, SiO_2(am) saturation, with a mean $\Delta_r G$ value of -0.5 ± 0.4 kJ.mol^{-1}, which has been calculated with respect to the whole dataset. As a consequence, and as also previously reported by Giammar et al. (2005) at 95 °C, it is very likely that the concentration of Si in the aqueous solutions was controlled by the solubility of amorphous silica, even if more accurate measurements would be needed to strengthen this statement (see section 3.2). It should be noted that all of the samples were supersaturated with respect to SiO_2(am) under ambient conditions (Table 3), given that the solubility of SiO_2(am) decreases with temperature. It is likely that the slight differences between the measured Si concentrations and the predicted Si equilibrium value results from minor precipitation of SiO_2(am) during the quench.

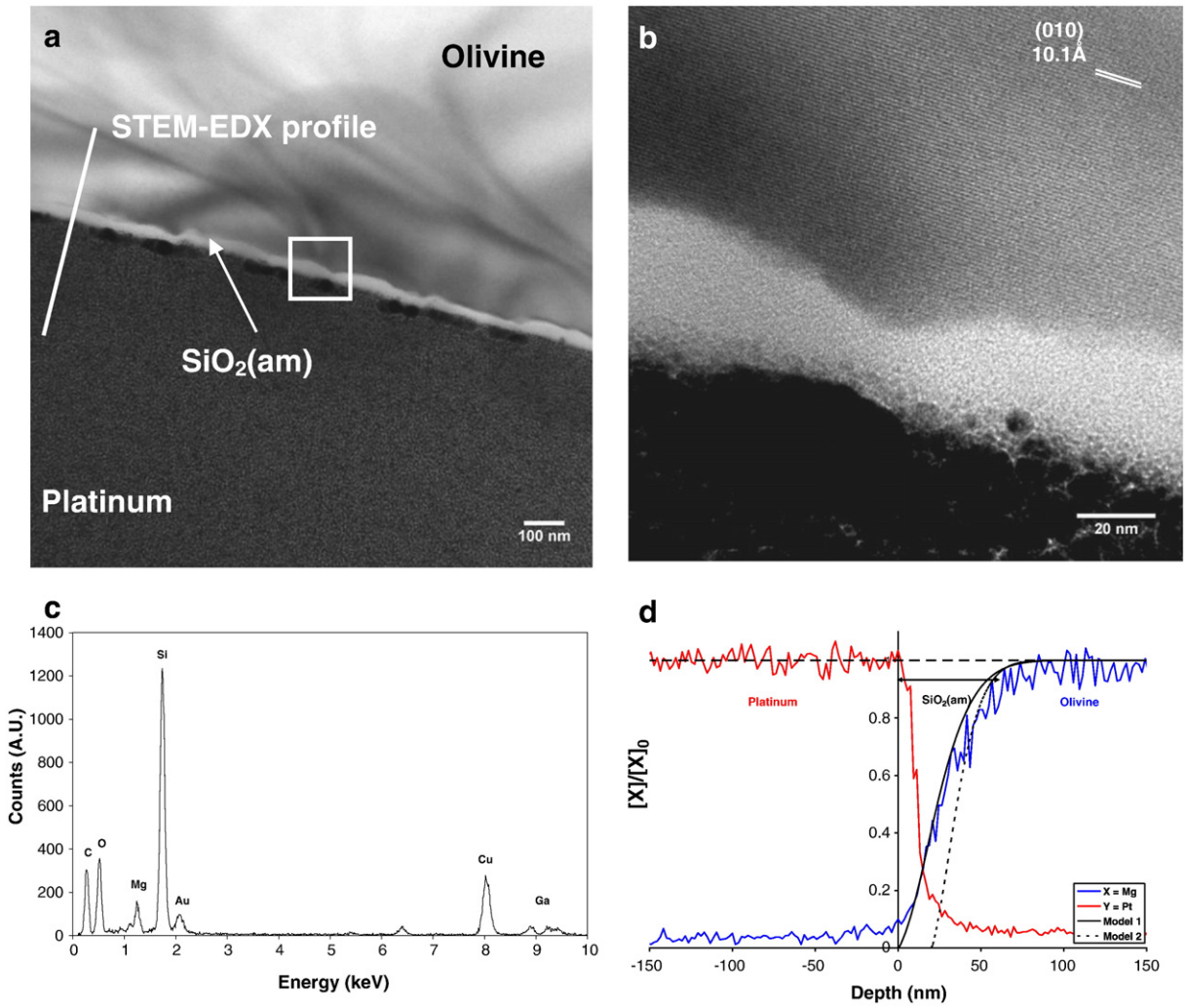

Fig. 2. TEM images and TEM-EDX measurements from the first FIB thin section realized on a single olivine grain from experiment 45-04. (a) Bright-field image of the interface at low magnification, showing a ubiquitous Si-rich layer contacting the pristine olivine, with an average thickness comprised between 15 and 40 nm. (b) HRTEM image of the area delimited by the square inset in a. Note the sharp but irregular termination of the lattice fringes of the olivine crystal at the crystal–amorphous interface. (c) Bulk EDX analysis of the Si-rich phase evidenced in a–b. Note the presence of small amounts of Mg incorporated within the Si-rich layer. (d) STEM-EDX profile realized along the line indicated in a. The red profile corresponds to the concentration profile of Pt (normalized to 1 in the Pt coating, located at the left hand side of the figure) and the blue profile represents Mg (normalized to 1 in olivine); the smooth curves (solid and dashed lines) represent results of diffusion modeling fitted to the experimental profile of Mg (see text and Appendix for details).

Interestingly, a similar range of Si concentrations was reported by Daval et al. (2009a), who used exactly the same experimental apparatus to study wollastonite carbonation under the same *P*–*T* conditions, whereas the formation of secondary SiO_2(am) phases was obvious (100 μm-thick coatings were observed). This comparison supports the idea that the apparent slight undersaturation of the solution with respect to SiO_2(am) is probably due to quenching effects.

3.2. Low SA/V experiment

The results of this experiment are summarized in Table 4. After a sharp rise of both the Mg and Si concentrations, the bulk fluid reached a steady-state composition after ~30 days, within experimental uncertainties (Fig. 4a). As illustrated in Fig. 4b, the release of Mg and Si was close to stoichiometry over the entire duration of the experiment. Conversely, one can calculate from the results listed in Table 4 that Fe release was not stoichiometric. As was discussed in section 3.1.1, this result could indicate the precipitation of secondary Fe(III)-rich phases.

The Mg and Si concentrations can be used to calculate the dissolution rate of olivine according to:

$$r_i(\bar{t}) = \frac{\Delta[i] \times m_{cell}(t-\Delta t)}{\Delta t \times m_0 \times SSA \times \eta_i} \quad (4)$$

In the above equation, $\Delta[i]$ is the difference in the concentrations of a solute i (Mg or Si; mol.kg^{-1}) for the samples recovered at time t and $t-\Delta t$, $m_{cell}(t-\Delta t)$ is the mass of aqueous solution remaining in the gold bag at time $t-\Delta t$ (just before sampling) and is expressed in kg, Δt (s) is the elapsed time between two samplings, m_0 is the initial mass of olivine (expressed in g), SSA (g.m^{-2}) is the specific surface area of olivine, and η_i is the stoichiometric coefficient of ith element in the mineral (1.82 for Mg; 1 for Si), so that $r_i(\bar{t})$ represents the average dissolution rate of olivine between two consecutive samplings. This value is determined with respect to the ith species of olivine, normalized to its surface area, and is thus expressed in mol.olivine.m^{-2}.s^{-1}. The dissolution rates of olivine with respect to Mg and Si, calculated according to Eq. (4), are plotted as a function of time in Fig. 4c. As can be seen, the dissolution rate of olivine monotonically decreased as a function of time throughout the

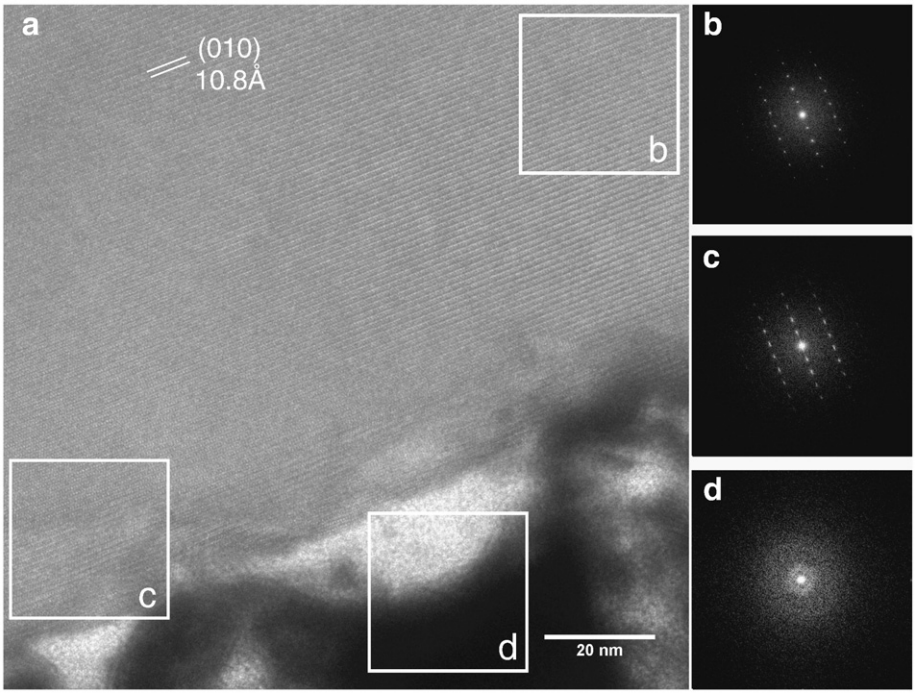

Fig. 3. TEM analysis of the second FIB thin section realized on the same olivine grain (i.e. Fig. 2) from experiment 45-04. (a) HRTEM image of the interface, showing disordering of the olivine network in the interfacial region. (b) FFT of the crystalline, unaltered olivine. (c) FFT of interfacial region (corresponding to the area labeled c in a). Note that the diffraction spots are broader, indicating disordering in this area. (d) FFT of the amorphous Si-rich layer.

experiment. At the end of the experiment, the dissolution rate of olivine was about two orders of magnitude slower than that determined at the beginning of the experiment. The decrease of the olivine dissolution rate as a function of time is in fact not surprising because the pH of the solution steadily increased as the reaction proceeded, due to the consumption of H^+ by the dissolution of olivine. To address the question whether the measured decrease in rates can be predicted using data from studies that determined the dependence of olivine dissolution rate on pH, the bulk solution pH was calculated with CHESS following the method described in section 2.4 for each of the recovered samples. The mean pH between two consecutive samples was set to equal the average pH determined from the solution chemistry of these two samples (for instance (see Table 4), from the chemical composition of samples OL-04 and OL-05, we calculated that the pH was respectively 3.88 and 3.96 after 1.94 and 2.95 days, so that the mean pH corresponding to the dissolution rate we reported for OL-05 is 3.92). The calculated dissolution rates are plotted as a function of the mean pH in Fig. 4d. Although the error bars for pH are quite large due to the sliding average method we adopted, two important observations can be emphasized: first, at the beginning of the experiments (corresponding to the more acidic pH conditions), both the pH-dependence and the absolute values of the dissolution rates are in reasonable agreement with the rate law from Rosso and Rimstidt (2000). Secondly, at pH values greater than 3.9, the sharp decrease of the dissolution rates measured in the present study cannot be attributed to pH only. Moreover, as mentioned in Table 4, all of the rates were obtained at Gibbs free energies less than

Table 4
Summary of the results obtained for the low *SA/V* experiment.

Sample	Time	m_{cell}	Si	Mg	Fe	log r_{Si}	log r_{Mg}	pH_{in}	pH_{ex}	ΔG_r(sil)	ΔG_r(for)	$\alpha(\bar{t})_{Si}$	$\alpha(\bar{t})_{Mg}$
	Days	g	mM	mM	mM	mol/m^2/s	mol/m^2/s			kJ/mol	kJ/mol		
OL-01	0.00	179.3	0.07	0.01	5.9E−05	n.c.	n.c.	3.11	n.c.	−13.27	−160.1	n.c.	n.c.
OL-02	0.13	174.4	0.24	0.26	3.6E−03	−7.22	−7.31	3.24	4.68	−9.65	−133.8	0.99	0.99
OL-03	0.93	165.4	0.91	1.30	8.2E−04	−7.42	−7.49	3.63	5.33	−5.84	−110.3	0.84	0.88
OL-04	1.94	160.8	1.64	2.58	7.0E−04	−7.51	−7.53	3.88	5.48	−3.84	−97.8	0.99	1.16
OL-05	2.95	157.2	1.97	3.18	8.7E−04	−7.87	−7.87	3.96	5.58	−3.28	−94.1	0.52	0.63
OL-06	4.87	154.1	2.37	3.82	7.4E−04	−8.07	−8.14	4.04	5.58	−2.72	−90.7	0.36	0.38
OL-07	6.83	150.1	2.63	4.39	2.3E−03	−8.27	−8.19	4.09	5.67	−2.41	−88.3	0.25	0.36
OL-08	10.95	146.9	3.17	5.80	9.6E−05	−8.30	−8.14	4.20	5.77	−1.85	−83.5	0.25	0.45
OL-09	16.93	144.1	3.66	6.63	1.2E−04	−8.50	−8.54	4.25	5.92	−1.41	−81.0	0.17	0.19
OL-10	23.85	141.8	3.79	7.13	8.2E−05	−9.17	−8.83	4.28	6.02	−1.31	−79.8	0.04	0.11
OL-11	32.93	138.9	3.93	7.68	d.l.	−9.26	−8.91	4.31	5.96	−1.20	−78.6	0.03	0.09
OL-12	52.05	136.2	4.67	8.07	1.1E−03	−8.86	−9.40	4.33	5.97	−0.67	−77.3	0.09	0.03
OL-13	58.91	133.0	4.70	8.04	1.2E−02	−9.88	n.c.*	4.32	5.92	−0.64	−77.4	0.01	n.c.

The first three columns indicate the name of the sample, the time duration after which it was taken and the mass of the solution in the cell after sampling. The three following columns contain, respectively, the aqueous concentrations of SiO_2(aq), Mg^{2+}, and Fe(aq) measured by ICP-MS (mmol.L^{-1}). The subsequent columns report the corresponding dissolution rates based either on Si or Mg concentrations. The columns labeled pH_{in} and pH_{ex} indicate, respectively, the calculated and measured pH for each sample. The two following columns gather the values of Gibbs free energy of dissolution (kJ.mol^{-1}) of forsterite and SiO_2(am) at T = 90 °C and pCO_2 = 20 MPa. The last columns report the values of $\alpha(\bar{t})$ as defined by Eq. (8). * not calculable, the concentration of Mg being greater in sample OL-12 than in sample OL-13.

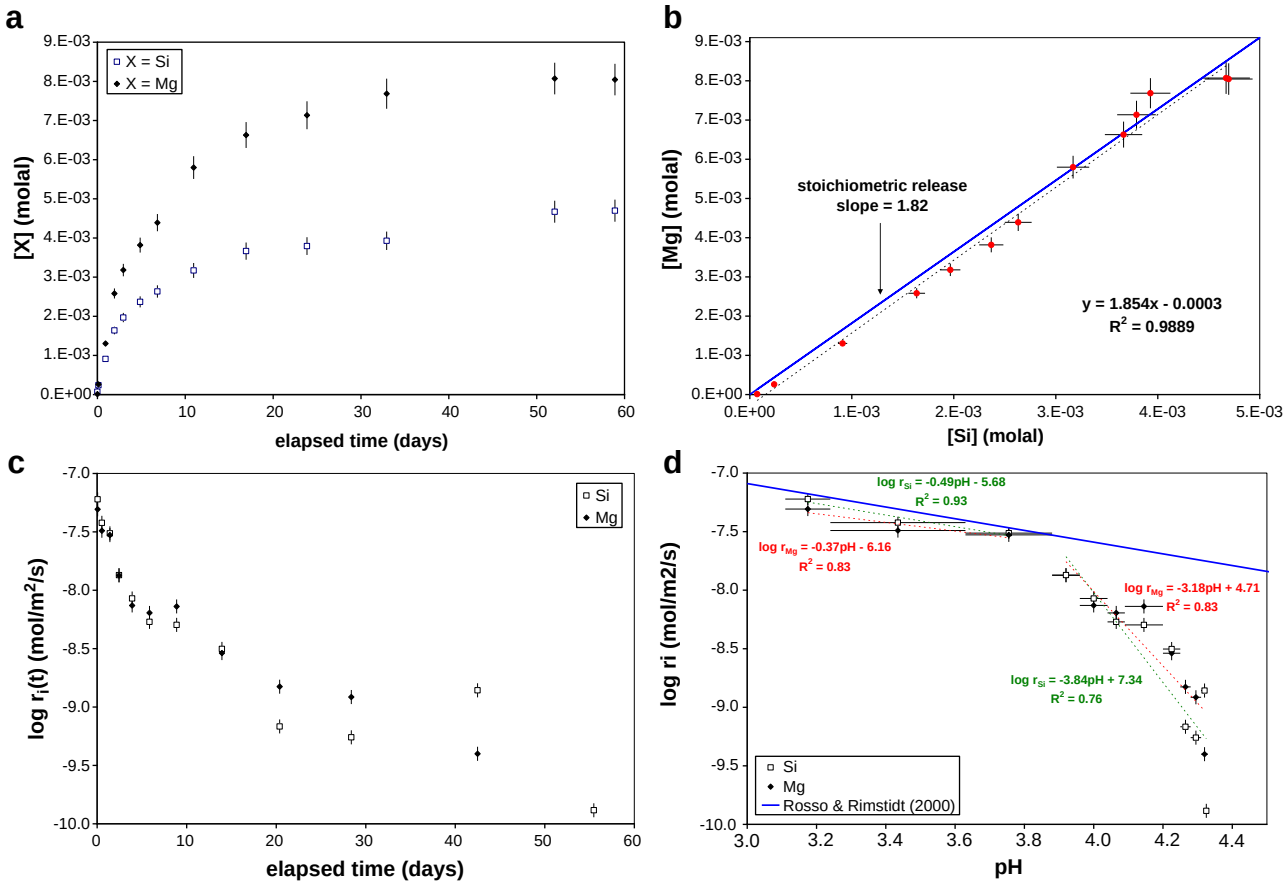

Fig. 4. Bulk aqueous chemistry measurements of the olivine dissolution rate for the low *SA/V* experiment. (a) Mg and Si concentrations of aliquots sampled in situ as a function of time. Note the attainment of a steady-state composition after 50 days of reaction, within experimental uncertainties. (b) Aqueous Mg concentrations plotted as a function of aqueous Si concentrations for the entire duration of the experiment. Dissolution was essentially stoichiometric, the slope of the linear regression (1.85) being very close to the stoichiometric slope of olivine (Mg/Si = 1.82). (c) Dissolution rate of olivine as a function of time, shown as a function of the Si and Mg (log) release rates. Note the continuous decrease of the rate over the duration of the experiment. (d) Dissolution rate of olivine reported as a function of pH. The solid blue line corresponds to the predicted rate using data from Rosso and Rimstidt (2000). At pH<3.9 our rate data are in good agreement with the predicted rate (blue line), whereas at higher pH the dissolution rate of olivine dramatically decreases, revealing a major discordance with the predicted rate (blue line).

-77.4 kJ.mol^{-1}, which corresponds to conditions usually referred to as 'far-from-equilibrium'. Understanding these results is one of the main objectives in the next section.

4. Discussion

The discussion that we present below is centered around four central themes. The first treats the discrepancy between the measured release of Mg and Si from olivine, and that predicted by geochemical modeling using rate laws published in the literature. The second theme explores reasons for this discrepancy. One possibility is that the creation of the amorphous silica layer ultimately controls olivine dissolution. Since it was impossible to define a rate of olivine dissolution for the high *SA/V* experiments because the Si and Mg concentrations achieved steady-state values after 1 day of reaction, the third theme therefore addresses alternative approaches to measuring olivine dissolution rates under such conditions. Finally, the last theme discusses how future research could elucidate more precisely the exact role that surface layers have on the dissolution of the parent mineral.

4.1. Dissolution of olivine: measured and predicted release of Mg and Si

The results of the high *SA/V* experiments suggest that at $T = 90$ °C and $pCO_2 = 25$ MPa, the carbonation process is slow: no carbonate minerals were evidenced in any of the 18 samples of this study, and the aqueous solutions were found to be saturated with respect to magnesite for one sample only. Qualitatively, this result is in fair agreement with Gerdemann et al. (2007), who showed that at $T = 95$ °C, the carbonation yields were no more than 3% in the most favorable of cases (i.e. when the reaction was initiated in alkaline solutions, with a particle grain size <37 μm). Consistent with these results, Giammar et al. (2005), who carried out carbonation experiments on 125–250 μm olivine powders at $T = 95$ °C and $pCO_2 = 100$ bar, reported that no carbonate minerals were identified after durations as long as 4 weeks. Therefore, the aim of the present section is to determine whether slow carbonation rates of olivine at 90–95 °C, while in qualitative agreement with the two aforementioned studies, can be predicted using published general kinetic rate laws that were developed for olivine dissolution at far-from-equilibrium conditions.

To realize this goal, the methodology successfully applied by Daval et al. (2009a) for describing the carbonation of wollastonite under similar conditions was adapted to the carbonation of olivine initiated in pure water equilibrated with an elevated pCO_2 (given that the experimental results are similar, no attempt was made to model the dissolution of olivine in saline solutions). The reaction shown below (based on pure forsterite in the code CHESS) describes the corresponding process, which is in agreement with the experimental results:

$$Mg_2SiO_4 + 4H^+ \rightarrow 2Mg^{2+} + zSiO_2(aq) + (1-z)SiO_2(am) + 2H_2O \quad (5)$$

In the above equation, z is a fractionation coefficient with a value between 0 and 1. The solution analyses (Table 3) suggest that the reaction proceeded close to SiO_2(am) saturation from the first day of the experiment. In agreement with this observation, Giammar et al. (2005) reported that the concentration of Si in the aqueous solutions was controlled by the solubility of amorphous silica. As a consequence, our aqueous data and observations showing the formation of a Si-rich layer on olivine surfaces (Fig. 2a), combined with the data from Giammar et al. (2005), support the assumption that the value of z is controlled by an instantaneous chemical equilibrium between the bulk solution and SiO_2(am) throughout the experiment. Because no other secondary phases were observed, amorphous silica was therefore the only solid allowed to precipitate in the numerical simulations discussed hereafter. We used olivine dissolution rate laws from 7 different far-from-equilibrium studies (Table 1), all performed in flow-through reactors (except that of Chen and Brantley, 2000) to test whether any of them could reproduce the experimentally measured release of Mg. For a given simulation, the modification of the speciation of the solution resulting from olivine dissolution is calculated at each time step, as thoroughly described in Daval et al. (2010a).

Fig. 5a compares the experimental data with the temporal evolution of Mg release from olivine using the 7 aforementioned rate studies. After 45 days of reaction, a 6-fold factor exists between the maximum and minimum concentrations (i.e. considering the rate laws determined by Rosso and Rimstidt (2000) and Hänchen et al. (2006), respectively). Such rate discrepancies are not rare among dissolution kinetics studies of a given mineral (e.g. see Hellmann (1994) for albite, Nagy (1995) for clay minerals), and can be ascribed to various factors, such as whether true steady state conditions were achieved, the number of runs performed to determine a rate law, the statistic treatment used for interpreting the raw data, uncertainties in normalization of the rates to the actual surface areas (which are subject to large errors), or the extent of the pH- and T-range used to establish the rate laws. The thorough statistical treatment of the data by Rosso and Rimstidt (2000) may make their rate law more reliable than those from other studies. Conversely, the T-range of their study is relatively limited (25–45 °C) compared to that of, e.g., Hänchen et al. (2006), such that the latter study may be more appropriate for extrapolation of rates to 90 °C. Thus, it is difficult to ascertain which study is best used for comparison with our data. The most important result shown in Fig. 5a is that after 45 days, there exists a 1.8 and 2.5 order of magnitude difference between the concentration of Mg released in the present experiments (mean value of 10.2 ± 3.7 mmolal) and the Mg concentrations extrapolated from the rates given in Rosso and Rimstidt (2000) and Hänchen et al. (2006), respectively.

We therefore ask which mechanisms are responsible for the large difference existing between our data and the numerical simulations. A close-up of the data in Fig. 5a, shown in Fig. 5b, suggests that the reaction takes place in two steps: during the first 24 h, the concentration of magnesium rose sharply, presumably in a similar way to the simulation based on the rate law of Rosso and Rimstidt (2000), and then the Mg concentration leveled off at a mean value of 10.2 ± 3.7 mmolal. Moreover, this value is close to that expected if a stoichiometric release of Mg and Si is assumed, and SiO_2(aq) is in equilibrium with SiO_2(am): $[Mg] = \eta_i \times [SiO_2(aq)]_{eq} = 10.1$ mmolal. This result points out that olivine dissolution may be controlled by the formation of the amorphous silica layer.

4.2. Rate-controlling step of olivine carbonation at 90 °C in closed systems

The easiest way to investigate the dissolution of olivine in batch reactors at conditions undersaturated with respect to SiO_2(am) is to run experiments with a low SA/V ratio. As outlined in section 3.2, at a low SA/V ratio the dissolution rate of olivine steadily decreased with time (Fig. 4c), this observation being partly explained by the increase in pH during the reaction (Fig. 4d). To highlight the influence of

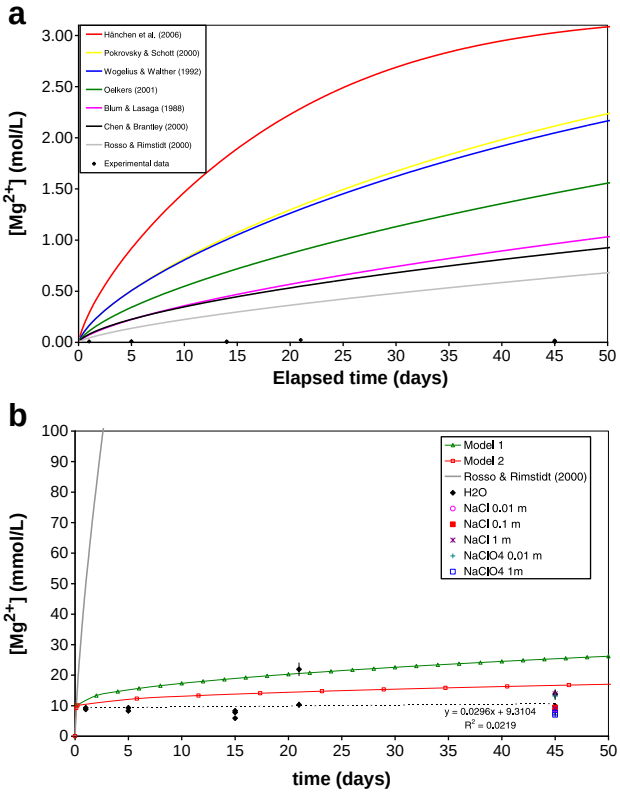

Fig. 5. (a) Kinetic modeling of olivine dissolution according to Eq. (5), using the CHESS code implemented with the rate law corresponding to Eq. (3b) and rate data from the literature (see Table 1). Because CHESS can only simulate the dissolution of pure forsterite, note that all the calculated concentrations were multiplied by 0.88, this corresponding to the stoichiometry of the San Carlos olivine we used. These simulations are compared with the results from the high SA/V experiment. (b) Close up showing the absence of the statistical evolution of the Mg concentrations during the experiment (dotted line). The solid lines with open triangles and squares represent the predicted evolution of Mg concentrations based on a process which becomes diffusion controlled as saturation of the bulk solution with respect to SiO_2(am) is reached. These curves were obtained independently from the solution analyses, and were not intended to finding the best fit to the Mg concentrations, but rather were intended for comparing the aqueous data to the evolution of Mg release predicted for a diffusion-limited process (see text and Appendix for details).

parameters other than pH (and T), we propose the following empirical expression for the dissolution rate law of olivine:

$$r_{Si,Mg}(\bar{t}) = k_{90} \times a_{H^+}(\bar{t})^n \times \alpha(\bar{t}) \quad (6)$$

where k_{90} corresponds to the rate constant of olivine dissolution at 90 °C (mol.m^{-2}.s^{-1}) and $\alpha(\bar{t})$ is a dimensionless attenuation term, which varies between 0 and 1, that accounts for the decrease of the dissolution rate due to the free energy, as well as any other parameters, excluding pH and T. It is worth noticing the similarities between this parameter and the $f(\Delta G_r)$ term used in general kinetic rate laws (e.g. Lasaga, 1995). However, at this stage, let us consider $\alpha(\bar{t})$ only as an undefined parameter that does not imply any specific mechanism.

At the beginning of the experiment, we pointed out that the first calculated rates were in fair agreement with extrapolations based on the rate law determined by Rosso and Rimstidt (2000). Because it is likely that only pH affected the very first rate data (the aqueous phase containing very low concentrations of dissolved Mg and Si, see Table 4 and corresponding values of ΔG_r(olivine)), we can reasonably set $\alpha(\bar{t})_0 = 1$ for the first rate data, so that Eq. (6) becomes:

$$r_{Si,Mg}(\bar{t})_0 = r_{Si,Mg}(\bar{t} = 0.07 \text{ days}) = k_{90} \times a_{H^+}(\bar{t} = 0.07 \text{ days})^n \quad (7)$$

Finally, the parameter k_{90} can be substituted in Eq. (6) by its value taken from Eq. (7), so that $\alpha(\bar{t})$ can be expressed as follows:

$$\alpha(\bar{t}) = \frac{r_{Si,Mg}(\bar{t})}{r_{Si,Mg}(\bar{t})_0} \times \left(\frac{a_{H^+}(\bar{t})_0}{a_{H^+}(\bar{t})}\right)^n \quad (8)$$

If one supposes, in agreement with most of olivine dissolution studies, that $n = 0.5$ (see Table 1), then the parameter $\alpha(\bar{t})$ can be calculated as a function of time from the data listed in Table 4.

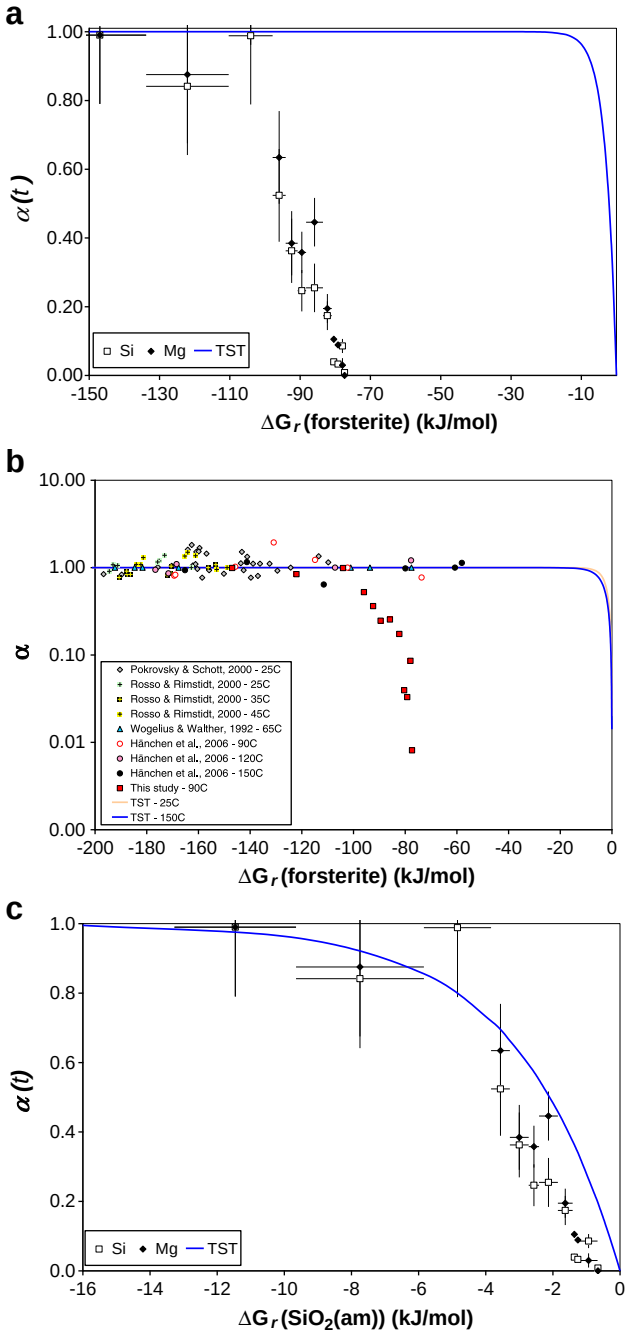

Fig. 6. Parameter $\alpha(\bar{t})$, as defined by Eq. (8), plotted as a function of (a) ΔG_r(olivine) and (c) $\Delta G_r(SiO_2(am))$. Each graph also shows curves based on TST. (b) Comparison of the parameter $\alpha(\bar{t})$ measured in the present study to that determined from published literature rate data. With respect to the published rate data, only rates obtained under conditions far-from-equilibrium with respect to SiO_2(am) saturation were considered. In general, the parameter $\alpha(\bar{t})$ can be thought of as a normalized rate.

In Fig. 6a, the parameter $\alpha(\bar{t})$ was plotted as a function of ΔG_r (olivine). The quite large error bars for ΔG_r(olivine) are due to the sliding average method we adopted, whereas the error bars for $\alpha(\bar{t})$ were mainly due to the pH intervals between times t and $t-\Delta t$. The value of $\alpha(\bar{t})$ decreases over a range in free energy where a simple TST rate equation does not predict any decrease of the rate. Moreover, if the rates of dissolution (normalized using the procedure outlined above for α) determined in the studies listed in Table 1 (all largely undersaturated with respect to SiO_2(am)) are plotted as a function of ΔG_r, these rates also do not show any decrease over this range (Fig. 6b). Moreover, the most interesting point arises from the plot of $\alpha(\bar{t})$ as a function of $\Delta G_r(SiO_2(am))$, shown in Fig. 6c. As can be seen in this figure, the normalized drop of olivine dissolution rate (i.e. $\alpha(\bar{t})$) tends to 0 as equilibrium with respect to SiO_2(am) is approached. Moreover, the dataset fits well to a simple TST rate equation of the form: $f(\Delta G_r) = 1 - \exp(\Delta G_r/RT)$, where $\Delta G_r = \Delta G_r(SiO_2(am))$. Whether this TST-like dependence is a fortuitous result or not cannot be ascertained in our study.

Considering the results discussed in section 4.1, and in agreement with previous studies which proposed that silica layers passivate the surface of olivine (e.g. Bearat et al., 2006), here we further propose that the dissolution rate of olivine is controlled by that of an interfacial Si-rich layer, such that Eq. (6) could be re-written as:

$$r_{Si,Mg}(\bar{t}) = k_{90} \times a_{H^+}(\bar{t})^n \times f(\Delta G_r(SiO_2(am))) \quad (9)$$

where $\alpha(\bar{t})$ was replaced by $f(\Delta G_r(SiO_2(am)))$, a function which describes the dependence of the dissolution rate of the silica surface layer in terms of the activity of SiO_2(aq). Indeed, as evidenced in Fig. 6c, one possibility is that such a function can be described by a TST relation: $f(\Delta G_r(SiO_2(am))) = 1 - exp(\Delta G_r(SiO_2(am))/RT)$. This until now unrecognized feedback between the bulk concentration of aqueous silica and the rate of olivine dissolution leads to a discussion of the following points:

(i) Although an overall kinetic relation given by Eq. (9) has never been proposed for olivine until now, it should be emphasized that similar relations have already been proposed for others phases. For instance, Berger et al. (2002) proposed that between 100 and 300 °C, the dissolution rate of sanidine feldspar is controlled by the concentration of SiO_2(aq) and thus, by the saturation index of a SiO_2 polymorph. With respect to multi-oxide glasses, the dissolution kinetics of both borosilicate and basaltic glasses were proposed to be intimately linked to that of a surface layer with a composition corresponding to (or close to) that of SiO_2(am) (e.g. Bourcier et al., 1990; Berger et al., 1994; Daux et al., 1997; Grambow and Muller, 2001; Gislason and Oelkers, 2003; for a thorough review of the rate laws proposed in these papers, see Gin et al., 2008).

(ii) It may be surprising that the phase which we propose to ultimately control the dissolution rate of olivine is neither present at the beginning of the reaction, nor is it thermodynamically predicted to form during the course of the experiment, because the fluid was undersaturated with respect to SiO_2(am) at all times. In spite of direct evidence of the formation of such a phase for this specific low *SA/V* experiment, several results from the literature are consistent with the occurrence of interfacial Si-rich layers at conditions nominally undersaturated with respect to SiO_2(am). For instance, Pokrovsky and Schott (2000a) measured that in acidic conditions and at ambient temperature, the surface of olivine consisted of a 2 nm-thick Si-rich layer supposedly formed by ion exchange between Mg^{2+} and H^+, followed by polymerization of the silica tetrahedrons. The occurrence of interfacial amorphous silica layers on olivine surface was recently confirmed by Tisserand and Hellmann (2008), who showed that the weathering of olivine at pH = 1 and

at room temperature resulted in the formation of a 5 nm-thick Si-rich layer, proposed to be formed by an interfacial dissolution–precipitation mechanism in a thin fluid-film contacting the olivine surface (i.e. in such a mechanism, it is the properties of the interfacial fluid, which are different from those of the bulk solution (i.e. local pH, dielectric constant, diffusion rate), that can lead to precipitation of a secondary phase in the thin interfacial fluid film, even though the bulk solution is undersaturated with respect to the same secondary phase).Regardless of the actual mechanism of formation of this Si-rich layer, the main point here is that the abovementioned observations, even though realized on olivine weathered at low temperature, support the idea that the dissolution of olivine promotes the formation of an amorphous silica interfacial phase, which would thus make feasible an olivine dissolution process controlled by such a phase.

(iii) An interesting point arises from a comparison of the release rates of Mg and Si (see Fig. 6c). Their aqueous ratios from nearly all of the measurements were stoichiometric with respect to olivine (Fig. 4b), such that the normalized rates determined using either Mg or Si are identical, within experimental uncertainties. This result may seem counter-intuitive: although a feedback between the release of Si, the aqueous Si concentration, and the presence of an interfacial Si-rich phase is reasonable (perhaps characterizable within the framework of TST), it is less obvious why the release of Mg should follow such a trend. A possible explanation for this observation is that the Si-rich layer (regardless of its mechanism of formation) is essentially non-porous and passivating. Thus, its continuous destruction (i.e. dissolution) is a necessary requirement for olivine dissolution to proceed unhindered. Following this proposition, the release of Mg from olivine is governed by the dissolution rate of the Si-rich layer, which progressively slows down as the concentration of SiO_2(aq) increases in the bulk solution. Thus, the dissolution rate of the silica layer is controlled by a chemical process (saturation index of bulk solution with respect to SiO_2(am)), whereas the release of Mg is controlled by a physical process (passivation effect), and its rate cannot exceed that of the Si-rich layer dissolution.

(iv) It is important to realize that the ideas proposed in the current section can only be justified with respect to olivine dissolution at the particular conditions used in the present study. At other conditions of dissolution these results may not at all be applicable. As an example, at higher temperatures and pH, published studies have demonstrated that although slowed down, the carbonation of olivine can reach high extents of reaction (e.g. Bearat et al., 2006; Gerdemann et al., 2007; Dufaud et al., 2009). It is thus obvious that in these studies the dissolution of olivine did not stop when the aqueous phase reached saturation with respect to SiO_2(am), meaning either that (1) the physical characteristics of the Si-rich layers are different (more porous) at higher temperature or (2) the alteration of olivine took place in these latter studies following a far slower mechanism (solid-state diffusion, see Putnis, 2009 for further details on the respective rates of hydrolysis vs. solid-state diffusion), which is activated at high temperature. Moreover, and perhaps most importantly, the conclusions reached in the present study should also not be applied *a priori* to other minerals. For instance, Daval et al. (2009a,b) demonstrated that wollastonite dissolution was not hindered by the formation of a SiO_2(am) layer, whereas the physico-chemical conditions of reaction were similar to those of the present study (same T and pCO_2, similar calculated pH range). These intriguing differences point out the need for more research in order to predict the feedback effects between silicate mineral dissolution and interfacial SiO_2(am)-like phase formation. This question is discussed in section 4.4.

Finally, to summarize points i–iv, we have proposed that in addition to the rate-controlling parameters determined in previous studies (pH, T, surface area), the dissolution rate of olivine was also controlled by the thermodynamic 'distance' from equilibrium with respect to SiO_2(am) and the passivating properties of the silica layer. The consequences of this with respect to olivine dissolution and CO_2 uptake in geologic sequestration context are potentially important. Among others, a question directly arising from this finding is the following: what happens during the olivine dissolution process when the bulk fluid reaches saturation with respect to SiO_2(am)? This case is encountered either in high *SA/V* scenarios of olivine dissolution, or after long durations of olivine/water interactions in confined environments. This question will be the main concern of the subsequent section.

4.3. Implications for long-term olivine–water–CO_2 interactions at 90 °C

One of the important points with respect to Mg release in the high *SA/V* experiments is the observation that after the initial rise, the Mg concentrations become constant in the fluid after 1 day (Fig. 5b). Whether Mg release still occurred after this is a question that cannot be answered in the present study. If yes, the errors in the measurements were presumably larger than any potential changes in Mg concentration, precluding the determination of Mg release rates based on the aqueous chemistry. Consequently, this section aims to estimate the maximum and minimum rates of Mg release for durations as long as 45 days during the course of the high *SA/V* experiments, following alternative strategies. The lower bound of the rate of the process is quite easy to fix: from what was pointed out in section 4.2, r_{Mg} may equal 0 when $\Delta G_r(SiO_2(am)) = 0$. This implies a completely impermeable olivine surface due to the silica layer. Insights into the upper bound of the release rate of Mg, corresponding to a residual alteration rate of olivine when the solution is saturated with respect to SiO_2(am), may benefit from the nanoscale analyses performed on the FIB thin sections described in section 3.1.1. Two different aspects of our observations can be used to propose a rough estimation:(i) The first estimation is based on the thickness of the layer evidenced in Fig. 2a. The assumption is made that (a) the whole layer was generated through an overall incongruent process, whereas the bulk solution was saturated with respect to SiO_2(am) (i.e. for $t \geq 1$ day) and (b) this overall process leads to a homogeneous layer 40 nm-thick. We know from previous studies (see section 4.2) that the first hypothesis is not exact, since a small fraction of the layer was presumably formed at conditions undersaturated with respect to SiO_2(am); the second hypothesis is not correct as well, as the thickness of the silica layer was shown to vary all along the olivine surface (Figs. 2a and 3a). However, because we aim at determining the *upper bound* of a residual alteration rate, the maximum thickness of the layer should be considered. Using such assumptions, the coating was thus generated progressively with time through an overall incongruent process, the external boundary of the Si-rich layer (formed at $t<1$ day) being stabilized (i.e. its dissolution ceased) when the bulk fluid reached saturation with respect to SiO_2(am). If one supposes that alteration process is transport-limited because the porosity of the silica layer is either small and/or poorly interconnected, then the thickness (d) of the layer would be controlled by a square root dependence with time (e.g. Corvisier et al., 2010, and references therein):

$$d = \varepsilon \times \sqrt{t} \tag{10}$$

Considering that after 45 days the thickness is 40 nm, then $\varepsilon = 5.9\ \text{nm.s}^{-1/2}$. The corresponding evolution of aqueous Mg concentrations during the course of the high *SA/V* experiments is shown in Fig. 5b. The modeled curve (solid line with open triangles) was built from the sum of the curve obtained using Rosso and Rimstidt (2000)

data for $[SiO_2(aq)]<[SiO_2(aq)]_{eq}$ and the transport limited curve predicted by Eq. (10) for $[SiO_2(aq)]>[SiO_2(aq)]_{eq}$. The overall curve is much closer to the data than any other curves shown in Fig. 5a. The best agreement is actually obtained with $d \sim 10$ nm ($\varepsilon = 1.5$ nm.s$^{-1/2}$), leading to [Mg] = 13.8 mmol.L^{-1} after 45 days (data not shown); however, this is not further considered here, as the primary goal of this section is to estimate an upper bound of the olivine alteration rate, and not the best fit of the aqueous concentration of Mg.

The approach described above can be used to estimate the time required for releasing an *ad hoc* amount of Mg (10%) from olivine. Such an extent translates into a silica layer 3.5 μm-thick, which would be formed in ~945 years following Eq. (10) and using $\varepsilon = 5.9$ nm.s$^{-1/2}$. This value of 945 years is about 5 orders of magnitude greater than that obtained following the simulation based on the far-from-equilibrium data of Hänchen et al. (2006) (one can calculate that 10% of olivine weathered corresponds to a Mg concentration in the aqueous phase of ~0.86 mol.L^{-1}, which is reached within ~3.7 days, according to the simulation reported in Fig. 5a), and 4 orders of magnitude greater than that obtained using the data of Rosso and Rimstidt (2000) (~56.8 days) for $0<t<45$ days.

(ii) The second estimation is based on the Mg profiles measured by STEM-EDX, shown in Fig. 2d. A typical Mg profile has sigmoidal behavior, but is most probably not representative of the true profile which is likely to be much sharper. An extended discussion of the nature of this profile is given in the Appendix. For over 30 years, it has been proposed that sigmoidal cation profiles are evidence for a solid-state interdiffusion mechanism, since these profiles could be qualitatively reproduced through diffusion modeling (Hellmann, 1997, see in addition, Hellmann et al., 2003, 2004). Solid-state diffusional transport is far slower than chemical hydrolysis reactions (see discussion of the rates of the respective mechanisms in, e.g. Putnis, 2009), and is likely to control the rates in our experiments, if one supposes that the amorphous Si-rich layers formed on olivine are non-porous (or the pores are not connected). The rate of this process can be estimated by fitting the Mg STEM-EDX profile, which can be reproduced using the general diffusion Eq. (11) below, the latter accounting for the outward diffusion of species within the silica layer (Doremus, 1975):

$$\frac{\partial C}{\partial t} = \frac{\partial}{\partial x}\left(\tilde{D}\frac{\partial C}{\partial x}\right) + a\left(\frac{\partial C}{\partial x}\right) \quad (11)$$

In this equation, t is time, C is the normalized concentration of the element chosen ([Mg]), x is the depletion depth (measured from the fluid–solid interface), $\tilde{D}$ a solid-state interdiffusion coefficient between Mg^{2+} and H^+ species (see Appendix), and a is the rate of retreat of the fluid–solid interface. The fitting procedure consisted in finding the value of $\tilde{D}$ which allowed the best agreement between the modeled and measured STEM-EDX Mg profile (black solid line in Fig. 2d, see Appendix for associated diffusion calculations). From this value, we calculated the expected evolution of both the cation depletion profile in the layer as a function of time and the resulting amount of Mg released into the fluid during the course of these high *SA/V* experiments (see Appendix and solid line with open squares in Fig. 5b). As before, we can use this approach to estimate the time required for the release of 10% of the Mg contained in olivine: ~2220 years, i.e. between 4 and 5 orders of magnitude greater than that obtained using the simulations based on Eq. (3b) and rate data of Rosso and Rimstidt (2000) or Hänchen et al. (2006), respectively. To further illustrate the overestimations caused by the use of classical geochemical codes in the context of carbon sequestration, we determined the time after which the solution would become supersaturated with respect to magnesite. According to CHESS calculations, magnesite saturation corresponds to [Mg] ~ 17.6 mmol.L^{-1}, which is reached within ~67 days according to diffusion modeling, that is, a time period dramatically longer than expected using the simulations based on rate data from Rosso and Rimstidt (2000) or Hänchen et al. (2006), respectively (between 2.5 and 3.5 orders of magnitude greater).

A final comment can be made on these estimations: there is a major conceptual difference between the approach adopted following (i) and that reported (and further described in the Appendix) following (ii). With respect to the first estimation, the assumption is made that the Si-rich coating is a distinct phase, potentially formed by an interfacial dissolution-precipitation mechanism (see Hellmann et al., 2003; Zhang and Luettge, 2009). Conversely, the second estimation presupposes that the Si-rich phase was (at least partly) formed by a solid-state diffusion mechanism. The intrinsic mechanism cannot be deduced from the present study, and needs to be addressed in future investigations (see also further discussion in the Appendix). However, it is worth noting that both models converge towards similar residual rates, which is the most important result of this study. Moreover, such estimated maximum rates are compatible with the fluid data.

To summarize this section, the lower bound of the rate can be assumed to equal 0. Despite the inherent uncertainties of the present data and their interpretation, it is reasonable to conclude that the upper bound of the dissolution rate of olivine may be up to 5 orders of magnitude slower than those predicted by conventional geochemical codes based on far-from-equilibrium rate data.

4.4. Understanding the physical and chemical properties of silica layers

The conclusion of the present study is quite straightforward: at 90 °C, and at elevated pCO_2 of ~20–25 MPa, the dissolution of forsterite olivine appears to be controlled by the saturation state of the fluid with respect to SiO_2(am) and the passivating properties of the amorphous silica layer. Starting from this assessment, one could think that obtaining more reliable simulations of fluid–rock interactions using reaction-transport codes for any silicate could simply be achieved by adding a specific dependence of the mineral dissolution rate law on the aqueous concentration of Si (or on the $\Delta G_r(SiO_2(am))$ parameter). However, such an approach would be at odds with results from e.g. Daval et al. (2009b), who showed that the occurrence of silica layers formed on the surface of wollastonite under similar conditions (same T and pCO_2) did not significantly affect its dissolution rate because of their meso-porous structure. Moreover, this approach would probably not be able to describe adequately the high extents of carbonation of olivine measured at higher temperature (e.g. Bearat et al., 2006; Gerdemann et al., 2007; Garcia et al., 2010), even though saturation with respect to SiO_2(am) was reached as well. Given that modeling of water–rock interactions (in particular related to CO_2 sequestration) relies on geochemical kinetic codes that generally do not account for the presence of passivating surface layers, future studies should be dedicated to understanding which parameter(s) and mechanisms are responsible for the non-universal transport properties of silica layers formed on mineral surfaces. Only such work will permit more accurate codes to be developed. To date, the treatment of minerals on a case-by-case basis emphasizes the fact that our understanding of these mechanisms is in its infancy.

The starting point for these future studies could be based on understanding the striking discrepancies evidenced between wollastonite and olivine reactivity. Assuming that a comparison of the reactivities of these two minerals makes sense presupposes that the silica layers formed on each one of these substrates originate from similar mechanisms. Although this statement would need to be rigorously confirmed, preservation of the original wollastonite morphology during the growth of silica layers (Huijgen et al., 2006; Daval et al., 2009a,b) suggests that, as for olivine, they are formed by an interfacial process. Moreover, as already emphasized elsewhere (e.g. Bunker, 1994; Cailleteau et al., 2008; Casey, 2008; Jollivet et al., 2008; Schott et al., 2009), surface silica layers should not be viewed as an inert material, but rather as phases that can undergo continuous

restructuring. As an example, Cailleteau et al. (2008) proposed that pore closure occurs subsequent to the progressive densification of the silica gel, via the condensation of silanol groups and the attainment of a Q^4 structure (i.e. a central SiO_4^{4-} entity connected to 4 other Si groups). Whether specific characteristics inherited from the parent phase influence these restructuring mechanisms is still an unresolved issue for silicate minerals.

The obvious differences between olivine and wollastonite, which may control the corresponding chemical and structural properties of the silica layers are: (1) their chemical composition (respectively, Mg–Fe-rich vs. Ca-rich), (2) their crystallography (olivine is an orthosilicate, composed of isolated SiO_4^{4-} tetrahedra, whereas wollastonite is an inosilicate, composed of SiO_4^{4-} tetrahedra linked in a single-chain structure), (3) their dissolution rates: at 90 °C and acidic pH, the far-from-equilibrium dissolution rate of wollastonite is approximately one order of magnitude greater than that of forsteritic olivine, see e.g. Guyot et al. (in press) for a review. A faster dissolution rate may exceed a characteristic time needed for amorphous silica rearrangement, polymerization, and pore closure. Stated another way, i.e., passivating properties are obtained when the rate of densification of the silica layer exceeds that of silicate hydrolysis. At this point, it is difficult to determine *a priori* which specific characteristic(s) can explain the observed differences between olivine and wollastonite reactivity, in particular in SiO_2(aq)-rich solutions. However, in our opinion, the 3rd point which suggests that the passivating ability of silica coatings depends on the differences between the inherent silicate dissolution and amorphous silica restructuration rates, may in fact be the parameter that deserves the most attention. This proposition potentially accounts for the differences observed between olivine and wollastonite reactivity, since wollastonite dissolves faster than olivine. Moreover, it has been recently found for olivine that at temperatures between 150 and 200 °C, the connectivity of Si tetrahedra within the amorphous Si-rich phase was Q^3, instead of Q^4 (Davis et al., 2009; King et al., 2010). The last step of the densification process, which leads to the passivating Q^4 structure, may compete with the formation of crystalline Q^3 phases such as serpentines (King et al., 2010). Considering all of these observations, it is of importance to correctly deconvolute the respective rates of silicate hydrolysis and silica densification in future experiments. This may be one of the key points to improving the accuracy of kinetic modeling of silicate dissolution reactions. Specific experiments similar to those described in the present study, but run with Fe-, Ca- and Mg-orthosilicate and inosilicate end-members should help to isolate one-by-one the abovementioned parameters.

5. Conclusions

The present study initially aimed at better understanding what controls olivine carbonation rates in confined environments and at temperatures relevant to CO_2 sequestration. In agreement with a growing number of studies, we have reached the conclusion that the dissolution of olivine is kinetically slowed down by the formation of amorphous silica layers. The presence of an amorphous silica layer, which apparently begins to form even when the solution is undersaturated with respect to SiO_2(am) (consistent with previous studies, e.g. Pokrovsky and Schott, 2000a; Tisserand and Hellmann, 2008), causes the dissolution rate of olivine to dramatically decrease. As shown by our kinetic analyses, the olivine dissolution rate at conditions when the solution is in equilibrium with amorphous silica cannot be exactly determined, but should lie between a minimum rate of zero and a maximum rate that is several (4–5) orders of magnitude less than the maximum rate at far-from-equilibrium conditions. This result emphasizes the fact that this effect should be added to the list of different mechanisms that potentially can retard the kinetics of mineral dissolution, such as the existence of a critical ΔG_r of reaction (e.g. free energy boundary value below which etch pits freely nucleate, see Lasaga and Luttge, 2001; Hellmann and Tisserand, 2006) or the inhibiting properties of Al(aq) on Al-silicate dissolution rates (Oelkers et al., 1994).

The above discussion points out that for reactive-transport codes to improve their predictive capabilities with respect to simulating fluid–rock interactions, surface interfacial processes must be correctly understood and integrated into these codes. With respect to CO_2 sequestration via mineral trapping, this study also suggests that at industrial scales of CO_2 injection, processes such as those proposed by Kelemen and Matter (2008) have clear advantages. Their methodology relies on a continuous renewal of fluids in contact with minerals, which prevents a decrease in the supply metal cations (Mg, Fe, Ca) due to mineral surface passivation. Ensuring a steady supply of these metal cations should theoretically ensure a high degree of metal carbonate formation and concomitant CO_2 sequestration.

Regarding the mechanisms responsible for developing passivating silica layers, a substantial amount of work will have to be achieved in order to develop better predictive models. In addition to carbonation experiments with Fe-, Ca- and Mg-orthosilicate and inosilicate end-members, supplementary flow-through experiments with controlled concentrations of added SiO_2(aq) are suggested in order to refine the trends observed in this study. Moreover, it may be possible that at challenging analytical conditions (i.e., when the aqueous ratio $\Delta[i]/[i]$ (i represents a released element) tends towards 0 as a solution reaches equilibrium with respect to SiO_2(am)), detailed nanoscale investigations of the reacted solids should help to determine the (possible) residual silicate alteration rate. Once the mechanisms responsible for rendering silica layer passivating are deciphered, a first step towards more predictive models may be based on defining pH–T–mineral conditions in which the $f(\Delta G_r)$ function of Eq. (3a) implemented in codes simply refers to the saturation state of the solution with respect to SiO_2(am).

Acknowledgments

This study would have not been possible without the technical assistance of N. Findling (ENS), J.-M. Guigner (IMPMC) and J.T. Larsen (LBNL) who are warmly acknowledged. DD is grateful to S. Gin, F. Brunet, G. Berger, P. Bénézeth, and J. Schott for the numerous and passionate discussions that contributed to this manuscript. The careful reviews and constructive comments by two anonymous reviewers and the editor (J. Fein) were also much appreciated for helping to improve the manuscript.

Appendix A

Calculation of the upper bound of Mg release rate, based on the STEM-EDXS profile of Mg

The chemical breakdown of minerals is generally governed by a sequential series of reaction and transport steps, the slowest step being rate-limiting for the overall process. Because while approaching saturation with respect to SiO_2(am), the hydrolysis rate of the surface silica layer tends towards 0 and the release rate of Mg drops accordingly, we suggest that olivine dissolution is no longer governed by hydrolysis reactions, but rather by diffusion through the surface layer. Moreover, if this layer is impermeable, the bulk solution does not contact the olivine surface anymore and a possible mechanism of transport of Mg is solid-state diffusion. Even though this type of diffusion can ensure a steady supply of Mg to the solution, it occurs at such a slow rate that it is analytically challenging to measure.

Using STEM-EDXS, we measured a ~50 nm-thick Mg profile at the interface which was sigmoidal. The question that arises as to whether the measured profile represents the true profile. The reliability of the Mg profile could have been considered as relatively accurate if the profile of the Pt coating that was applied before the FIB section was

made had been sharp. Instead, it was spread out over a thickness of ~25 nm (Fig. 2d). The estimated spatial resolution of STEM-EDXS analyses is on the order of 2–3 nm, and thus the sigmoidal nature of the Pt profile cannot be attributed to analytical limitations. Nonetheless, many other analytical factors can play a role with respect to both the Pt and Mg profiles (e.g. the FIB thin section was perhaps not rigorously orientated perpendicular to the EDXS detector of the microscope). In any case, it is certain that the true Mg profile is sharper than what is shown in Fig. 2d. Nonetheless, even when the Mg profile is adjusted to take into account the non-vertical nature of the Pt profile, the Mg profile is still not vertical, such that the Mg gradient is approximately 20–30 nm wide. On the one hand, it can be thought of as representing a step function-like profile that has been slightly broadened, again due to analytical considerations (orientation of FIB section, orientation of olivine-silica interface). Alternatively, the Mg profile can be considered to be truly sigmoidal. The former interpretation (step function profile) would be in agreement with an interfacial dissolution-reprecipitation process (Hellmann et al., 2003, 2004), whereas the latter (sigmoidal profile) would be indicative of a solid-state diffusion process. In addition to these interpretations, we cannot discount a mixed mechanism whereby the layer is originally created by a dissolution–reprecipitation process, but then as the layer's structure evolves with time (e.g. by pore closure, densification), the layer becomes passivating, such that the only process that allows reactant products to reach the bulk solution is by solid state diffusion. The different features of the TEM observations may be used to support either one of the two mechanisms. On the one hand, the hummocky nature of the amorphous silica layer shown in Fig. 3a speaks in favor of an interfacial precipitate. Conversely, the progressive structural modification from the bulk crystal to the amorphous silica (Fig. 3b–d) could actually be rather representative of a leached layer.

On the whole, the exact mechanism of how silica layers form during olivine dissolution cannot be unambiguously deciphered from the results obtained in the present study, but the most important result is that they rapidly evolve into a passivating structure that dramatically slows down the rate of olivine dissolution. Therefore, it is worth estimating a Mg release rate based on a solid-state diffusion mechanism because to the best of our knowledge, no previous studies have quantified the decrease of olivine dissolution rates due to the formation of Si-rich layers. In addition, the vast majority of CO_2 sequestration simulations used rate laws that did not take into account a potential passivation effect (e.g. Knauss et al., 2005; Xu et al., 2004, 2005; Gherardi et al., 2007). Thus, despite the uncertainties inherent to our assumptions and the calculations shown below, the rates that we deduce are most probably much closer to the actual weathering rate of olivine that occurs in confined environments, as compared to predicted rates based on far-from-equilibrium dissolution rates.

Referring back to Eq. (11), the parameter a was set to 0 because as proposed above, the outer interface of the assemblage (i.e. the fluid/silica interface) should remain in chemical equilibrium when the fluid reaches saturation with respect to SiO_2(am). In addition, the diffusion equation is assumed to satisfy the following boundary conditions (note that concentrations are normalized to that in the bulk olivine): at $x=0$, $C=0$, and at $x=\infty$ (the silica layer/bulk interface), $C=1$ and $\partial C/\partial x=0$. These boundary conditions are in good agreement with the measured chemical profiles of Mg; see also additional details in Hellmann (1997). The interdiffusion coefficient is defined as (see Daval et al., 2009b and references therein for details):

$$\tilde{D} = \frac{D_{Mg}D_H(C+1)^2}{4D_{Mg}C + D_H(1-C)} \tag{A1}$$

D_H and D_{Mg} are the individual diffusion coefficients of H^+ and Mg^{2+} species, respectively. For the sake of simplicity, note that pure forsterite is considered in the simulations hereafter. Eq. (11) was then linearized and solved numerically using a finite-volume approach and implicit–explicit discretization (see details in Daval et al., 2009b). The best fit of the measured profile was obtained with $D_H = 10^{-18}$ cm^2.s^{-1} and $D_{Mg} = 3.10^{-18}$ cm^2.s^{-1} (the corresponding simulation being the black solid line in Fig. 2d). Note that if one supposes that the actual profile is sharper than measured (~30 nm gradient instead of ~50 nm, i.e., after Pt profile correction applied), the values of D_H and D_{Mg} remain of the same order of magnitude ($D_H = 5.10^{-19}$ cm^2.s^{-1} and $D_{Mg} = 10^{-18}$ cm^2.s^{-1}, dashed line in Fig. 2d). Note that the use of these latter values would have not significantly changed the release rate of Mg (data not shown).

The values $D_H = 10^{-18}$ cm^2.s^{-1} and $D_{Mg} = 3.10^{-18}$ cm^2.s^{-1} were then used to estimate the release rate of Mg when limited by solid-state diffusion. The model was realized with the method described in Daval et al. (2009b), using $N=500$ meshes with a total length of $l=25$ μm (i.e., a large enough depth so that the concentrations of Mg in the deeper meshes remained numerically unaffected by the diffusion process, thus verifying the boundary conditions at the silica-olivine interface: $C=1$ and $\partial C/\partial x=0$). The generated profiles as a function of time were then recovered for further exploitation, as detailed hereafter. If one supposes that the olivine grains are perfect spheres with a mean radius of $r_{ol}=100$ μm (corresponding to the mean radius of the grains used for the high SA/V experiments), then the volume V_i of each spherical corona with width $\frac{l}{N}$ can be calculated using the following system of equations:

$$\begin{cases} V_{i=1}^{ext} = \frac{4}{3}\pi r_{ol}^3 ; V_i^{ext} = \frac{4}{3}\pi\left(r_{ol} - \frac{i-1}{N}\times l\right)^3, \forall i \in [2,N] \\ V_i^{int} = \frac{4}{3}\pi\left(r_{ol} - \frac{i}{N}\times l\right)^3 \\ V_i = V_i^{ext} - V_i^{int} \end{cases} \tag{A2}$$

From this system, the mass of a given corona m_i can be calculated supposing that its specific density is a linear combination between that of olivine (ρ_{ol}) and that of the hydrated amorphous silica (ρ_{sil}) which results from the exchange between H^+ and Mg^{2+}:

$$m_i = V_i.(C_i.\rho_{ol} + (1-C_i).\rho_{sil}) \tag{A3}$$

where C_i is the normalized concentration of Mg in the depleted layer at depth x. The molecular weight of a given corona can be inferred from the concentration of Mg in this layer, such that one can calculate the amount of Mg in this corona ($n_{Mg^{2+},i}$), based on the equation:

$$n_{Mg^{2+},i} = 2\times C_i \times \frac{m_i}{2.C_i.M_{Mg} + M_{Si} + 4.M_O + 4.(1-C_i).M_H} \tag{A4}$$

where M_{Mg}, M_{Si}, M_O, and M_H correspond to the molecular weights of Mg, Si, O, and H respectively. Then, the total amount of magnesium $n_{Mg^{2+},TOT}$ still present in the solid assemblage (i.e. olivine + leached layer) can be calculated according to:

$$n_{Mg^{2+},TOT} = \sum_{i=1}^{N} n_{Mg^{2+},i} + \frac{8}{3}\pi.(r_{ol}-l)^3 \times \frac{\rho_{ol}}{M_{ol}} \tag{A5}$$

where M_{ol} stands for the molecular weight of olivine (pure forsterite). Finally, the normalized extent of olivine weathering (ξ_n, corresponding to Mg release) can be calculated from the initial amount of magnesium present in an unweathered grain:

$$\xi_n = 1 - n_{Mg^{2+},TOT} \times \frac{3.M_{ol}}{8\pi.\rho_{ol}.r_{ol}^3} \tag{A6}$$

The results of these simulations are shown in Fig. 7, for an extent of magnesium depletion comprised between 0 and 10%. The thickness of the generated cation-depleted profiles, arbitrarily defined as the part

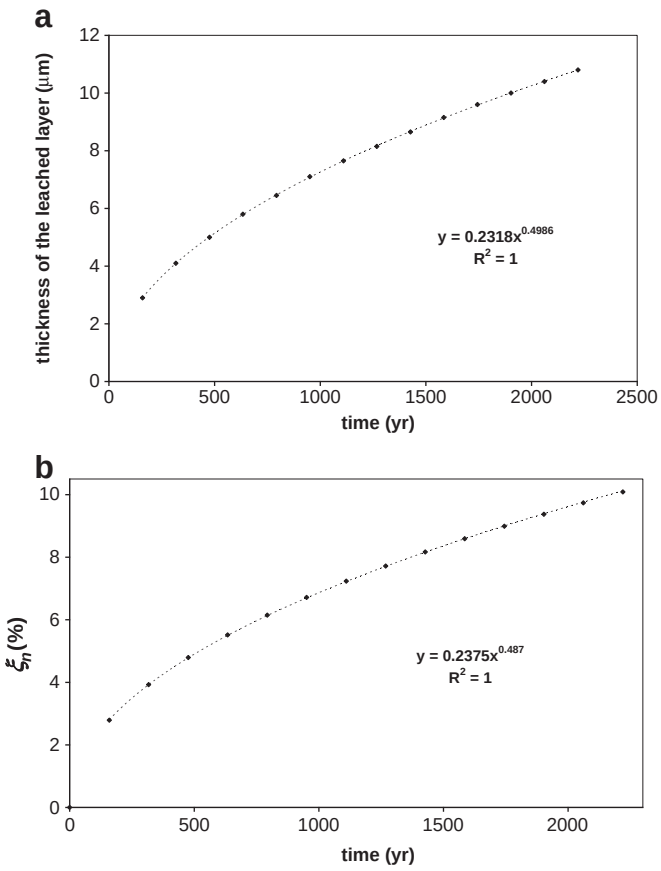

Fig. 7. Results of solid-state diffusion modeling using parameters determined experimentally for the diffusion coefficients of Mg and H. (a) Thickness of the leached layer (defined as a phase containing no more than 99.5% of Mg present in olivine) plotted as a function of time. The regressed line shows that the thickness of the layer increases as a function of the square root of the time, as expected for processes controlled by diffusion. (b) Extent of olivine dissolution as a function of time. The same characteristics as already described for the thickness of the Si-rich layer can be evidenced.

of the profile for which C_i<0.995, is shown in Fig. 7a. Not surprisingly, these data perfectly fit to a power regression of thickness as a function of time, with a value of the exponent close to 0.5, which is characteristic of a diffusion process where the thickness varies as a square root of time. The corresponding evolution of ξ_n as a function of time is shown in Fig. 7b. Again, the data provide a good fit with a square root trend. As can be seen, ξ_n equals 0.1 for time durations as long as ~2220 years, i.e. between 4 and 5 orders of magnitude greater than what was predicted from CHESS simulations (see section 4.3).

Finally, it is interesting to assess the aqueous Mg concentrations predicted for the duration of the high *SA/V* experiments following such an approach. The corresponding results are shown in Fig. 5b (the extent of olivine weathering was easily converted into aqueous Mg concentration based on the volume of the solution and the mass of the powder). As can be seen, the modeled curve (solid line with open squares), representing the sum of the curve obtained using Rosso and Rimstidt (2000) data for $[SiO_2(aq)]<[SiO_2(aq)]_{eq}$ and the transport-limited curve derived from Eq. (11) for $[SiO_2(aq)]>[SiO_2(aq)]_{eq}$ (i.e. when the solution is supersaturated with respect to SiO_2(am)), is compatible with the experimental dataset, with the expected evolution of Mg concentration being close to what we actually measured.

References

Andreani, M., Luquot, L., Gouze, P., Godard, M., Hoise, E., Gibert, B., 2009. Experimental study of carbon sequestration reactions controlled by the percolation of CO_2-rich brine through peridotites. Environmental Science & Technology 43, 1226–1231.

Awad, A., Koster van Groos, A.F., Guggenheim, S., 2000. Forsteritic olivine: effect of crystallographic direction on dissolution kinetics. Geochimica et Cosmochimica Acta 64, 1765–1772.

Bachu, S., 2000. Sequestration of CO_2 in geological media: criteria and approach for site selection in response to climate change. Energy Conversion and Management 41, 953–970.

Ballirano, P., De Vito, C., Ferrini, V., Mignardi, S., 2010. The thermal behaviour and structural stability of nesquehonite, MgCO3 center dot 3 H(2)O, evaluated by in situ laboratory parallel-beam X-ray powder diffraction: new constraints on CO_2 sequestration within minerals. Journal of Hazardous Materials 178, 522–528.

Bearat, H., McKelvy, M.J., Chizmeshya, A.V.G., Gormley, D., Nunez, R., Carpenter, R.W., Squires, K., Wolf, G.H., 2006. Carbon sequestration via aqueous olivine mineral carbonation: role of passivating layer formation. Environmental Science & Technology 40, 4802–4808.

Behar, F., Beaumont, V., Penteado, H.L.D., 2001. Rock-Eval 6 technology: performances and developments. Oil & Gas Science and Technology-Revue De L Institut Francais Du Petrole 56, 111–134.

Beinlich, A., Austrheim, H., Glodny, J., Erambert, M., Andersen, T.B., 2010. CO_2 sequestration and extreme Mg depletion in serpentinized peridotite clasts from the Devonian Solund basin, SW-Norway. Geochimica et Cosmochimica Acta 74, 6935–6964.

Berger, G., Claparols, C., Guy, C., Daux, V., 1994. Dissolution rate of a basalt glass in silica-rich solutions — implications for long-term alteration. Geochimica et Cosmochimica Acta 58, 4875–4886.

Berger, G., Beaufort, D., Lacharpagne, J.C., 2002. Experimental dissolution of sanidine under hydrothermal conditions: mechanism and rate. American Journal of Science 302, 663–685.

Blum, A., Lasaga, A., 1988. Role of surface speciation in the low-temperature dissolution of minerals. Nature 331, 431–433.

Bourcier, W.L., Peiffer, D., Knauss, K.G., McKeegan, K., Smith, D., 1990. A kinetic model for borosilicate glass dissolution based on the dissolution affinity of a surface reaction layer. Materials Research Society Symposium Proceedings, vol. 176, pp. 209–216. Scientific Basis for Nuclear Waste Management XIII.

Bunker, B.C., 1994. Molecular mechanisms for corrosion of silica and silicate-glasses. Journal of Non-Crystalline Solids 179, 300–308.

Cailleteau, C., Angeli, F., Devreux, F., Gin, S., Jestin, J., Jollivet, P., Spalla, O., 2008. Insight into silicate-glass corrosion mechanisms. Nature Materials 7, 978–983.

Casey, W.H., 2008. Glass and mineral corrosion dynamics and durability. Nature Materials 7, 930–932.

Chen, Y., Brantley, S.L., 2000. Dissolution of forsteritic olivine at 65 °C and 2<pH<5. Chemical Geology 165, 267–281.

Chen, Z.Y., O'Connor, W.K., Gerdemann, S.J., 2006. Chemistry of aqueous mineral carbonation for carbon sequestration and explanation of experimental results. Environmental Progress 25, 161–166.

Corvisier, J., Brunet, F., Fabbri, A., Bernard, S., Findling, N., Rimmele, G., Barlet-Gouedard, V., Beyssac, O., Goffe, B., 2010. Raman mapping and numerical simulation of calcium carbonates distribution in experimentally carbonated Portland-cement cores. European Journal of Mineralogy 22, 63–74.

Daux, V., Guy, C., Advocat, T., Crovisier, J.L., Stille, P., 1997. Kinetic aspects of basaltic glass dissolution at 90 degrees C: role of aqueous silicon and aluminium. Chemical Geology 142, 109–126.

Daval, D., Martinez, I., Corvisier, J., Findling, N., Goffe, B., Guyot, F., 2009a. Carbonation of Ca-bearing silicates, the case of wollastonite: experimental investigations and kinetic modeling. Chemical Geology 265, 63–78.

Daval, D., Martinez, I., Guigner, J.M., Hellmann, R., Corvisier, J., Findling, N., Dominici, C., Goffe, B., Guyot, F., 2009b. Mechanism of wollastonite carbonation deduced from micro- to nanometer length scale observations. American Mineralogist 94, 1707–1726.

Daval, D., Hellmann, R., Corvisier, J., Tisserand, D., Martinez, I., Guyot, F., 2010a. Dissolution kinetics of diopside as a function of solution saturation state: macroscopic measurements and implications for modeling of geological storage of CO_2. Geochimica et Cosmochimica Acta 74, 2615–2633.

Daval, D., Testemale, D., Recham, N., Tarascon, J.M., Siebert, J., Martinez, I., Guyot, F., 2010b. Fayalite (Fe2SiO4) dissolution kinetics determined by X-ray absorption spectroscopy. Chemical Geology 275, 161–175.

Davis, M.C., Brouwer, W.J., Wesolowski, D.J., Anovitz, L.M., Lipton, A.S., Mueller, K.T., 2009. Magnesium silicate dissolution investigated by Si-29 MAS, H-1-Si-29 CPMAS, Mg-25 QCPMG, H-1-Mg-25 CP QCPMG NMR. Physical Chemistry Chemical Physics 11, 7013–7021.

Doremus, R.H., 1975. Interdiffusion of hydrogen and alkali ions in a glass surface. Journal of Non-Crystalline Solids 19, 137–144.

Dufaud, F., Martinez, I., Shilobreeva, S., 2009. Experimental study of Mg-rich silicates carbonation at 400 and 500 degrees C and 1 kbar. Chemical Geology 265, 79–87.

Garcia, B., Beaumont, V., Perfetti, E., Rouchon, V., Blanchet, D., Oger, P., Dromart, G., Huc, A.Y., Haeseler, F., 2010. Experiments and geochemical modelling of CO_2 sequestration by olivine: potential, quantification. Applied Geochemistry 25, 1383–1396.

Gerdemann, S.J., O'Connor, W.K., Dahlin, D.C., Penner, L.R., Rush, H., 2007. Ex situ aqueous mineral carbonation. Environmental Science & Technology 41, 2587–2593.

Gherardi, F., Xu, T.F., Pruess, K., 2007. Numerical modeling of self-limiting and self-enhancing caprock alteration induced by CO_2 storage in a depleted gas reservoir. Chemical Geology 244, 103–129.

Giammar, D.E., Bruant, R.G., Peters, C.A., 2005. Forsterite dissolution and magnesite precipitation at conditions relevant for deep saline aquifer storage and sequestration of carbon dioxide. Chemical Geology 217, 257–276.

Gin, S., Jegou, C., Frugier, P., Minet, Y., 2008. Theoretical consideration on the application of the Aagaard–Helgeson rate law to the dissolution of silicate minerals and glasses. Chemical Geology 255, 14–24.

Gislason, S.R., Oelkers, E.H., 2003. Mechanism, rates, and consequences of basaltic glass dissolution: II. An experimental study of the dissolution rates of basaltic glass as a function of pH and temperature. Geochimica et Cosmochimica Acta 67, 3817–3832.
Gislason, S.R., Wolff-Boenisch, D., Stefansson, A., Oelkers, E.H., Gunnlaugsson, E., Sigurdardottir, H., Sigfusson, B., Broecker, W.S., Matter, J.M., Stute, M., Axelsson, G., Fridriksson, T., 2010. Mineral sequestration of carbon dioxide in basalt: a pre-injection overview of the CarbFix project. International Journal of Greenhouse Gas Control 4, 537–545.
Grambow, B., Muller, R., 2001. First-order dissolution rate law and the role of surface layers in glass performance assessment. Journal of Nuclear Materials 298, 112–124.
Guyot, F., Daval, D., Dupraz, S., Martinez, I., Menez, B., Sissmann, O., in press. CO_2 geological storage: the environmental mineralogy perspective. Comptes Rendus Geoscience. doi:10.1016/j.crte.2010.12.007.
Hänchen, M., Prigiobbe, V., Storti, G., Seward, T.M., M., M., 2006. Dissolution kinetics of fosteritic olivine at 90–150°C. Geochimica et Cosmochimica Acta 70, 4403–4416.
Hänchen, M., Prigiobbe, V., Baciocchi, R., Mazzotti, M., 2008. Precipitation in the Mg-carbonate system — effects of temperature and CO_2 pressure. Chemical Engineering Science 63, 1012–1028.
Hellmann, R., 1994. The albite–water system: part I. The kinetics of dissolution as a function of pH at 100, 200 and 300 °C. Geochimica et Cosmochimica Acta 58, 595–611.
Hellmann, R., 1997. The albite–water system.4. Diffusion modeling of leached and hydrogen-enriched layers. Geochimica et Cosmochimica Acta 61, 1595–1611.
Hellmann, R., Tisserand, D., 2006. Dissolution kinetics as a function of the Gibbs free energy of reaction: an experimental study based on albite feldspar. Geochimica et Cosmochimica Acta 70, 364–383.
Hellmann, R., Penisson, J.-M., Hervig, R.L., Thomassin, J.-H., Abrioux, M.-F., 2003. An EFTEM/HRTEM high-resolution study of the near surface of labradorite feldspar altered at acid pH: evidence for interfacial dissolution-reprecipitation. Physics and Chemistry of Minerals 30, 192–197.
Hellmann, R., Penisson, J.-M., Hervig, R.L., Thomassin, J.-H., Abrioux, M.F., 2004. Chemical alteration of feldspar: a comparative study using SIMS and HRTEM/EFTEM. In: Wanty, R.B., Seal II, R.R. (Eds.), Water Rock Interaction. A.A. Balkema, pp. 753–756.
Hellmann, R., Daval, D., Tisserand, D., 2010. The dependence of albite feldspar dissolution kinetics on fluid saturation state at acid and basic pH: progress towards a universal relation. Comptes Rendus Geoscience 342, 676–684.
Huijgen, W.J.J., Witkamp, G.-J., Comans, R.N.J., 2006. Mechanisms of aqueous wollastonite carbonation as a possible CO_2 sequestration process. Chemical Engineering Science 61, 4242–4251.
Jarvis, K., Carpenter, R.W., Windman, T., Kim, Y., Nunez, R., Alawneh, F., 2009. Reaction mechanisms for enhancing mineral sequestration of CO_2. Environmental Science & Technology 43, 6314–6319.
Jollivet, P., Angeli, F., Cailleteau, C., Devreux, F., Frugier, P., Gin, S., 2008. Investigation of gel porosity clogging during glass leaching. Journal of Non-Crystalline Solids 354, 4952–4958.
Jonckbloedt, R.C.L., 1998. Olivine dissolution in sulphuric acid at elevated temperatures — implications for the olivine process, an alternative waste acid neutralizing process. Journal of Geochemical Exploration 62, 337–346.
Kelemen, P.B., Matter, J., 2008. In situ carbonation of peridotite for CO_2 storage. Proceedings of the National Academy of Sciences of the United States of America 105, 17,295–17,300.
King, H.E., Plumper, O., Putnis, A., 2010. Effect of secondary phase formation on the carbonation of olivine. Environmental Science & Technology 44, 6503–6509.
Knauss, K.G., Copenhaver, S.A., 1995. The solubility of p-xylene in water as a function of temperature and pressure and calculated thermodynamic quantities. Geochimica et Cosmochimica Acta 59, 2443–2448.
Knauss, K.G., Johnson, J.W., Steefel, C.I., 2005. Evaluation of the impact of CO_2, co-contaminant gas, aqueous fluid and reservoir rock interactions on the geologic sequestration of CO_2. Chemical Geology 217, 339–350.
Lafargue, E., Marquis, F., Pillot, D., 1998. Rock-Eval 6 applications in hydrocarbon exploration, production, and soil contamination studies. Revue De L Institut Francais Du Petrole 53, 421–437.
Lasaga, A.C., 1981. Transition state theory. In: Lasaga, A.C., Kirkpatrick, R.J. (Eds.), Kinetics of Geochemical Process. Mineralogical Society of America.
Lasaga, A.C., 1995. Fundamental approaches in describing mineral dissolution and precipitation rates. In: White, A.F., Brantley, S.L. (Eds.), Chemical Weathering Rates of Silicate Minerals. Mineralogical Society of America.
Lasaga, A.C., Luttge, A., 2001. Variation of crystal dissolution rate based on a dissolution stepwave model. Science 291, 2400–2404.
Lee, M.R., Brown, D.J., Smith, C.L., Hodson, M.E., Mackenzie, M., Hellmann, R., 2007. Characterization of mineral surfaces using FIB and TEM: a case study of naturally weathered alkali feldspars. American Mineralogist 92, 1383–1394.
Liu, Y., Olsen, A.A., Rimstidt, J.D., 2006. Mechanism for the dissolution of olivine series minerals in acidic solutions. American Mineralogist 91, 455–458.
Luce, R.W., Bartlett, R.W., Parks, G.A., 1972. Dissolution kinetics of magnesium silicates. Geochimica et Cosmochimica Acta 36, 33–50.
Nagy, K.L., 1995. Dissolution and precipitation kinetics of sheet silicates. Chemical Weathering Rates of Silicate Minerals 31, 173–233.
O'Connor, W.K., Dahlin, D.C., Rush, G.E., Dahlin, C.L., Collins, W.K., 2002. Carbon dioxide sequestration by direct mineral carbonation: process mineralogy of feed and products. Minerals & Metallurgical Processing 19, 95–101.
Oelkers, E.H., 2001. An experimental study of forsterite dissolution as a function of temperature, and aqueous Mg and Si concentration. Chemical Geology 175, 485–494.
Oelkers, E.H., Schott, J., 2005. Geochemical aspects of CO_2 sequestration. Chemical Geology 217, 183–186.
Oelkers, E.H., Schott, J., Devidal, J.-L., 1994. The effect of aluminum, pH, and chemical affinity on the rates of aluminosilicate dissolution reactions. Geochimica et Cosmochimica Acta 58, 2011–2024.
Oelkers, E.H., Gislason, S.R., Matter, J., 2008. Mineral carbonation of CO_2. Elements 4, 333–337.
Pokrovsky, O.S., Schott, J., 2000a. Forsterite surface composition in aqueous solutions: a combined potentiometric, electrokinetic, and spectroscopic approach. Geochimica et Cosmochimica Acta 64, 3299–3312.
Pokrovsky, O.S., Schott, J., 2000b. Kinetics and mechanism of forsterite dissolution at 25 °C and pH from 1 to 12. Geochimica et Cosmochimica Acta 64, 3313–3325.
Prigiobbe, V., Costa, G., Baciocchi, R., Hanchen, M., Mazzotti, M., 2009. The effect of CO_2 and salinity on olivine dissolution kinetics at 120 °C. Chemical Engineering Science 64, 3510–3515.
Putnis, A., 2009. Mineral replacement reactions. Thermodynamics and Kinetics of Water–Rock Interaction 70, 87–124.
Rosso, J.J., Rimstidt, D.J., 2000. A high resolution study of forsterite dissolution rates. Geochimica et Cosmochimica Acta 64, 797–811.
Saldi, G.D., Jordan, G., Schott, J., Oelkers, E.H., 2009. Magnesite growth rates as a function of temperature and saturation state. Geochimica et Cosmochimica Acta 73, 5646–5657.
Schott, J., Pokrovsky, O.S., Oelkers, E.H., 2009. The link between mineral dissolution/precipitation kinetics and solution chemistry. Thermodynamics and Kinetics of Water–Rock Interaction 70, 207–258.
Seyfried, W.E., Gordon, P.C., Dickson, F.W., 1979. New reaction cell for hydrothermal solution equipment. American Mineralogist 64, 646–649.
Sidhu, P.S., Gilkes, R.J., Cornell, R.M., Posner, A.M., Quirk, J.P., 1981. Dissolution of iron-oxides and oxyhydroxides in hydrochloric and perchloric acids. Clays and Clay Minerals 29, 269–276.
Spycher, N., Pruess, K., Ennis-King, J., 2003. CO_2–H_2O mixtures in the geological sequestration of CO_2. I. Assessment and calculation of mutual solubilities from 12 to 100 °C and up to 600 bar. Geochimica et Cosmochimica Acta 67, 3015–3031.
Tisserand, D., Hellmann, R., 2008. Bridging the 'gap' between laboratory dissolution and natural chemical weathering. Geochimica et Cosmochimica Acta 72, A948.
van der Lee, J., De Windt, L., 2002. CHESS Tutorial and Cookbook. . Updated for version 3.0., Paris.
Wogelius, R.A., Walther, J.V., 1991. Olivine dissolution at 25 °C: effects of pH, CO_2, and organic acids. Geochimica et Cosmochimica Acta 55, 943–954.
Wogelius, R.A., Walther, J.V., 1992. Olivine dissolution kinetics at near-surface conditions. Chemical Geology 97, 101–112.
Xu, T., Apps, J.A., Pruess, K., 2004. Numerical simulation of CO_2 disposal by mineral trapping in deep aquifers. Applied Geochemistry 19, 917–936.
Xu, T.F., Apps, J.A., Pruess, K., 2005. Mineral sequestration of carbon dioxide in a sandstone–shale system. Chemical Geology 217, 295–318.
Zhang, L., Luettge, A., 2009. Theoretical approach to evaluating plagioclase dissolution mechanisms. Geochimica et Cosmochimica Acta 73, 2832–2849.